ARTICLE

Epigenetic loss of AOX1 expression via EZH2 leads to metabolic deregulations and promotes bladder cancer progression

Venkatrao Vantaku[1] · Vasanta Putluri[2] · David A. Bader [1] · Suman Maity[3] · Jing Ma[4] · James M. Arnold[5] ·
Kimal Rajapakshe[1] · Sri Ramya Donepudi[2] · Friedrich-Carl von Rundstedt[6,7] · Vaishnavi Devarakonda[8] ·
Julien Dubrulle[1,2] · Balasubramanyam Karanam[9] · Sean E. McGuire[1] · Fabio Stossi[1,2] · Abhinav K. Jain[10] ·
Cristian Coarfa [1,2] · Qi Cao [11] · Andrew G. Sikora[2,12] · Hugo Villanueva[2,12] · Shyam M. Kavuri[8] · Yair Lotan [13] ·
Arun Sreekumar[1,2,5] · Nagireddy Putluri[1,2]

Abstract

Advanced Bladder Cancer (BLCA) remains a clinical challenge that lacks effective therapeutic measures. Here, we show that distinct, stage-wise metabolic alterations in BLCA are associated with the loss of function of aldehyde oxidase (AOX1). AOX1 associated metabolites have a high predictive value for advanced BLCA and our findings demonstrate that AOX1 is epigenetically silenced during BLCA progression by the methyltransferase activity of EZH2. Knockdown (KD) of AOX1 in normal bladder epithelial cells re-wires the tryptophan-kynurenine pathway resulting in elevated NADP levels which may increase metabolic flux through the pentose phosphate (PPP) pathway, enabling increased nucleotide synthesis, and promoting cell invasion. Inhibition of NADP synthesis rescues the metabolic effects of AOX1 KD. Ectopic AOX1 expression decreases NADP production, PPP flux and nucleotide synthesis, while decreasing invasion in cell line models and suppressing growth in tumor xenografts. Further gain and loss of AOX1 confirm the EZH2-dependent activation, metabolic deregulation, and tumor growth in BLCA. Our findings highlight the therapeutic potential of AOX1 and provide a basis for the development of prognostic markers for advanced BLCA.

These authors contributed equally: Venkatrao Vantaku, Vasanta Putluri

✉ Nagireddy Putluri
putluri@bcm.edu

1 Department of Molecular and Cellular Biology, Baylor College of Medicine, Houston, TX, USA

2 Dan L. Duncan Cancer Center, Advanced Technology Core, Alkek Center for Molecular Discovery, Baylor College of Medicine, Houston, TX, USA

3 Department of Biostatistics, School of Public Health, University of Texas, Houston, TX, USA

4 Fred Hutchinson Cancer Research Center, Division of Public Health Sciences, Seattle, WA, USA

5 Verna and Marrs McLean Department of Biochemistry and Molecular Biology, Baylor College of Medicine, Houston, TX, USA

6 Scott Department of Urology, Baylor College of Medicine, Houston, TX, USA

7 Department of Urology, Jena University Hospital, Friedrich-Schiller-University, Jena, Germany

8 Lester and Sue Smith Breast Center, Baylor College of Medicine, Houston, TX, USA

9 Department of Biology and Center for Cancer Research, Tuskegee University, Tuskegee, AL, USA

10 Center for Cancer Epigenetics, Department of Epigenetics and Molecular Carcinogenesis, The University of Texas M. D. Anderson Cancer Center, Houston, TX, USA

11 Center for Inflammation and Epigenetics, Institute for Academic Medicine Houston Methodist Research Institute, Houston, TX, USA

12 Department of Otolaryngology-Head & Neck Surgery, Baylor College of Medicine, Houston, TX, USA

13 Department of Urology, University of Texas Southwestern, Dallas, TX, USA

Introduction

Urinary bladder cancer (BLCA) is the ninth most common cancer worldwide and is more prevalent in men [1]. The

American Cancer Society estimated about 81,190 new cases of bladder cancer and about 17,240 deaths from bladder cancer occurred in the United States in 2018 [2]. Low-grade tumors are generally noninvasive and carry a low risk of progression though disease recurrence is frequent. However, high-grade papillary tumors and carcinoma in situ are associated with a high risk of recurrence and disease progression, warranting close surveillance and intravesical therapy. Monitoring and repeated treatment, accounts for the relatively high cost of BLCA management compared to other cancers [3]. Molecular studies of non-muscle-invasive urothelial carcinoma of the bladder (NMIBC) have clearly shown the effects of genomic instability, chromosomal alterations, and allelic loss on the development and progression of BLCA [4, 5]. However, the metabolic changes associated with these genetic aberrations remain unknown. Here, we aimed to understand the potential metabolic dysregulations resulting from chromatin alterations that trigger the advanced bladder carcinogenesis.

Aldehyde oxidase 1 (AOX1) is a phase I xenobiotic enzyme that belongs to the xanthine oxidase family of cytosolic molybdoenzymes [6, 7]. AOX1 plays an important role in xenobiotic and drug metabolism by catalyzing the oxidation of endogenous and exogenous aldehydes and aromatic N-heterocycles [8]. Previous metabolomic analyses have shown altered patterns in phase I/II metabolism and the adverse effects of methylation-driven gene silencing on xenobiotic metabolism in BLCA tissues [9]. Promoter hypermethylation is a common mechanism for transcriptional silencing of tumor suppressor genes, such as *RB1* and *p16INK4A* [10–12]. Enhancer of Zeste homolog 2 (EZH2), an enzymatic subunit of the polycomb repressive complex 2 (PRC2), catalyzes methylation to induce chromatin compaction and transcriptional silencing [13]. Consistent with its previously known function as an epigenetic silencer in tumorigenesis and tumor progression [14], we sought to examine the role of EZH2 in *AOX1* silencing during BLCA progression.

In this study, we show that *AOX1* is epigenetically silenced by EZH2-mediated chromatin alterations in its promoter. Loss of AOX1 resulted in distinct metabolic alterations that are highly predictive of the different stages of BLCA progression. In normal bladder epithelial cells, knockdown of AOX1 led to the activation of the tryptophan-kynurenine pathway. This resulted in elevated nicotinamide-adenine dinucleotide phosphate (NADP) levels, which enhanced carbon flux via the pentose phosphate pathway (PPP), nucleotide synthesis and cell invasion. Ectopic expression of AOX1 in cancer cells resulted in decreased PPP metabolic flux, cell invasion, and nucleotide synthesis. Also, ectopic AOX1 expression reduced tumor xenograft growth in mice, possibly via a reduction in

nucleotide synthesis. Together, our findings suggest a novel oncogenic role for AOX1 in BLCA progression, suggest a metabolic basis for early tumor detection, and targeted therapies for BLCA.

Results

Detection of stage-specific metabolic alterations and risk prediction of BLCA tissues

To identify key altered metabolic pathways at different stages of BLCA, we analyzed metabolomic data collected from BLCA tissue samples obtained from the University of Texas Southwestern Medical Center, Dallas (clinical information in Supplementary Table 1). A total of 94 metabolites showed significantly altered levels in stages T1 to T4 compared with the Ta stage (Fig. 1a). Interestingly, a subset of the altered metabolites was associated with reactions catalyzed by AOX1 (Fig. 1a). A network-based pathway enrichment method NetGSA was [15] used to identify several enriched biochemical pathways such as nicotinamide, glycolysis, fatty acid, purine, and pyrimidine metabolism (Fig. 1b). These identified pathways were associated with several metabolic reactions catalyzed by AOX1 (Fig. 1c). Integration of metabolomics mapped genes from our study and transcriptomics from TCGA data revealed that AOX1 ranked second in the list of genes downregulated in cancer (Supplementary Fig. 2a). We analyzed the predictive power of the identified stage-specific BLCA-associated metabolites in an independent tissue cohort for validation. We used 119 tissue specimens collected at three institutions (clinical information in Supplementary Table 2). We selected a subset of seven metabolites (nicotinamide, methyl adenosine, asparagine, methyl histidine, indolacetaldehyde, tyrosine, and gentisatealdehyde) associated with AOX1 metabolic pathways and calculated the activity scores for each pathway based on Z-score transformed data. The activity score represents the likelihood that a metabolic pathway is active inside the cell and provides a basis for comparing metabolic pathway activities. A logistic regression model was used to build a classifier using activity scores derived from a training dataset comprised of two-thirds of the tissue samples ($n = 80$, randomly selected). We validated the predictive performance of the classifier by applying it to the remaining one-third of the samples ($n = 39$). The resultant receiver operating characteristic (ROC) curve was statistically significant ($p = 0.023$) with an area under curve (AUC) value of 0.689 (Fig. 1d). These results suggest AOX1-associated, stage-specific metabolites can be used as reliable prognostic markers for BLCA.
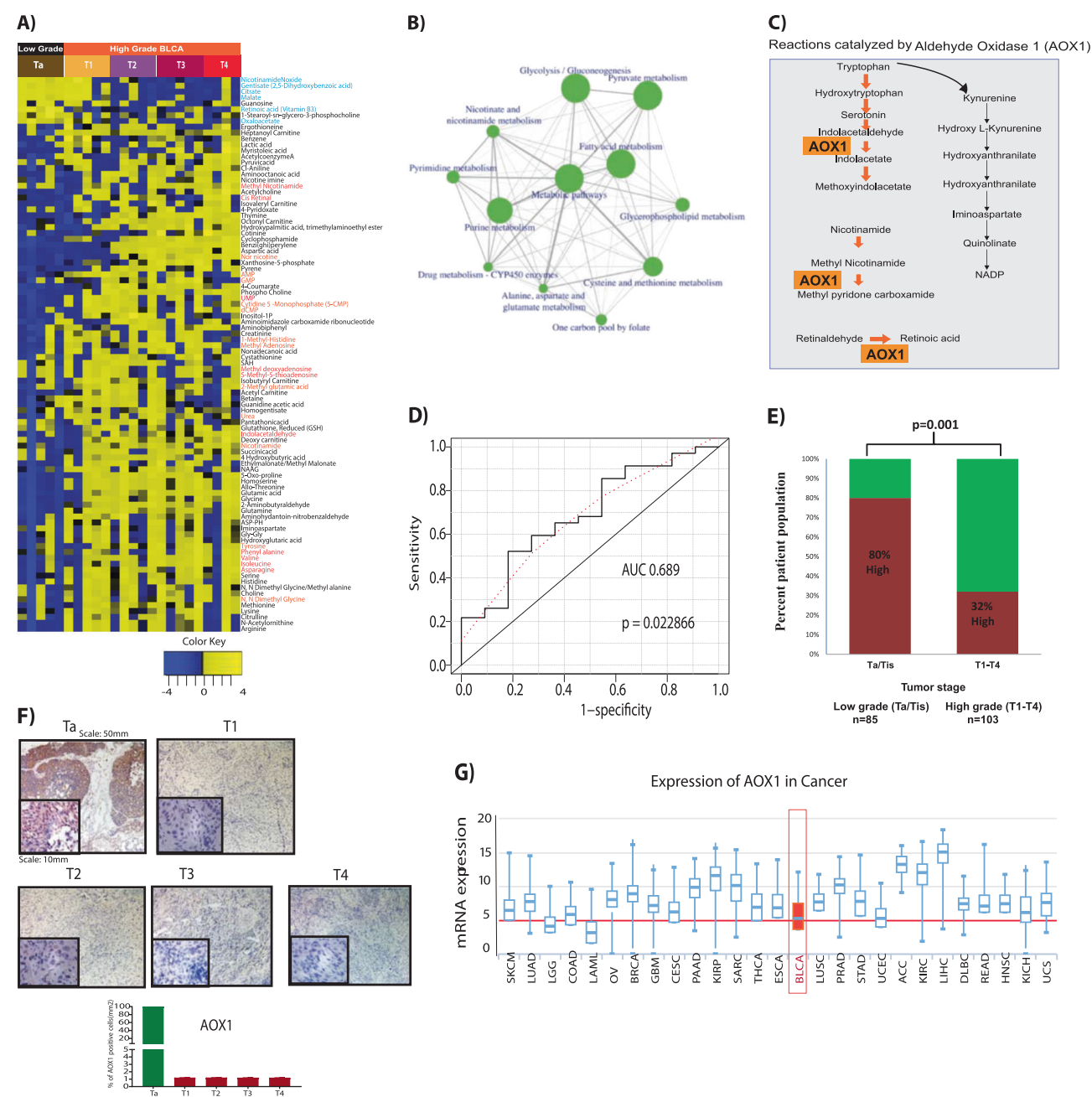
Fig. 1 Metabolic analysis of different-staged tissues, alterations in the AOX1-associated pathways and AOX1 expression in BLCA. **a** Heat map of hierarchical clustering of 95 differential metabolites from 25 BLCA tissue samples at different stages of BLCA. Columns represent individual tissue samples arranged according to BLCA stage, and rows represent distinct metabolites. Shades of yellow and blue represent higher and lower levels of metabolites, respectively, relative to the median metabolite levels (false discovery rate, FDR < 0.25). **b** Network representation of pathways (solid green colored circles: enriched pathways after integrative analysis using combined gene/metabolite-derived enrichment scores) altered in aggressive BLCA (stage Ta vs stages T1–T4). Arrow thickness correlates with the number of interacting components between two pathways. **c** Overview of metabolic pathway reactions associated with AOX1 (indicator represents exact reaction catalyzed by AOX1 in the pathway). **d** The plot describes the ROC based on the overall activity score for a select group of AOX1 associated metabolites ($n = 7$) in the logistic regression which yields a significant p-value ($p = 0.03$) with an AUC of 0.689. **e** Tissue microarray analysis of AOX1 expression comparing low-grade (Ta-Tis) and high-grade (T1-T4) BLCA. The scores of 0–3 were considered low and scores from 4 to 8 were considered high. The score represents a combination of staining intensity and percentage of tumor cells showing protein expression. **f** Representative photomicrograph of AOX1 immunostaining in stages Ta, T1, T2, T3, and T4 of BLCA. The bar graphs show relative AOX1 expression levels for the same slides. For normalization, AOX1 staining of Ta was used as 100% and AOX1 expression in other stages are shown as relative percentages. **g** Photographic representation of AOX1 mRNA expression in all cancers in TCGA dataset

AOX1 is significantly downregulated during BLCA progression

Our computational analysis suggested AOX1 may be a useful biomarker for BLCA progression. To examine this idea further, we used a tissue microarray to evaluate AOX1 expression in 188 human BLCA tissue samples at varying cancer stages. Low-grade (stages Ta and Tis) BLCA tissue specimens had higher AOX1 protein expression than high-grade (stages T1–T4) BLCA tissues (Fig. 1e). Immunohistochemical analysis also showed AOX1 downregulation in high-grade BLCA tissues (Fig. 1f). A comparison of AOX1 mRNA expression in the TCGA dataset revealed that BLCA had the lowest AOX1 mRNA expression levels across all cataloged tumors (Fig. 1g). AOX1 expression was lower in high-grade BLCA cell lines (UMUC3, J82, and T24) than low-grade RT4 BLCA cells, suggesting AOX1 expression may be lost during BLCA progression (Supplementary Fig. 1a). Analysis of data from public BLCA cohorts (Kim [16], TCGA [17], Sanchez [18]) showed significantly lower expression of AOX1 in cancerous tissue compared with normal bladder tissue (Supplementary Fig. 2b, c). Moreover, analysis of AOX1-associated substrate metabolites (Supplementary Fig. 3a) and product metabolites (Supplementary Fig. 3b) coupled with the AOX1 expression pattern suggest AOX1 levels decrease during BLCA progression.

AOX1 is silenced by EZH2

To determine if AOX1 loss during BLCA progression is controlled by epigenetic regulation, we treated UMUC3 cells with methyltransferase inhibitors, 5-aza-2′-deoxycytidine (AZA) and Adenosine dialdehyde (Adox). Both AZA and Adox treatments resulted in increased mRNA and protein expression of AOX1. Treatment of UMUC3 cells with Trichostatin A, a histone deacetylase inhibitor, had no effect (Fig. 2a and Supplementary Fig. 4a), suggesting AOX1 expression in these cells was suppressed by methylation. To identify the methyltransferase(s) responsible for silencing the AOX1 locus, we performed a correlation analysis of AOX1 with EZH2, DNMT1, DNMT3A, or DNMT3B, using data from public cohorts (TCGA [17], Choi [19], Kim [16], and Sanchez [18]). We observed a strong negative correlation between AOX1 and EZH2 in all cohorts (Fig. 2b, c). In addition, we found the potential methylated CpG islands at the AOX1 promotor region (Supplementary Fig. 5a) and have moderate negative correlation of DNMT3B with AOX1where as DNMT1 and DNMT3A showed no correlation with AOX1 (Supplementary Fig. 5b).

To examine the regulatory relationship between EZH2 and AOX1, we treated, UMUC3 BLCA cells, with a highly selective pharmacological EZH2 inhibitor GSK126 [20], and found the increase in AOX1 expression. (Fig. 2d).

Next, we examined AOX1 and EZH2 protein expression in BLCA specimens and found that EZH2 expression increased while AOX1 expression decreased in a stage-dependent manner (Fig. 2e). Moreover, EZH2 knockdown resulted in a significant increase of AOX1 expression in UMUC3 and T24 cells (Fig. 2f, g).

EZH2 alters chromatin structure at the AOX1 promoter locus

EZH2 regulates epigenetic silencing by methylation of histone H3 on lysine 27 (H3K27) at the gene promoter locus [20] or controls DNA methylation [21]. To determine the mechanism by which EZH2 silenced AOX1 expression, we performed bisulfite sequencing and chromatin immunoprecipitation (ChIP) experiments. Stage-specific DNA from BLCA tissues were used for bisulfite conversion and pyrosequencing. We observed high levels of methylation at the AOX1 promoter locus in stage T1–T4 BLCA tissues. Methylation was absent at the AOX1 promoter locus in benign, normal, and Ta tissues (Fig. 3a). We performed ChIP assays to assess enrichment of EZH2 and H3K27me3 at the AOX1 promoter in EZH2 knockdown and GSK126-treated BLCA cells. Quantitative real-time PCR (ChIP-qPCR) was used to measure the H3K27 trimethylation and EZH2 occupancy at the AOX1 promoter locus. EZH2 levels were significantly reduced at the AOX1 promoter locus in EZH2 knockdown cells, but remained unchanged in GSK126-treated cells. However, both EZH2 knockdown and GSK126-treated BLCA cells showed a significant reduction in H3K27 trimethylation at the AOX1 promoter, which correlated with increased AOX1 expression in these cells (Fig. 3b).

Next, we examined the role of EZH2 methyltransferase activity in AOX1 silencing. We transfected normal immortalized bladder epithelial cells (SV-HUC-1) with adenovirus constructs expressing wild type EZH2 and a mutant version of EZH2 (ΔSET) that had a truncated C-terminal SET domain and lacked methyltransferase activity [22]. SV-HUC-1 cells that expressed wild type EZH2 showed decreased AOX1 mRNA and protein levels compared with control cells. In contrast, cells expressing the ΔSET construct showed no significant decrease in AOX1 mRNA and protein levels (Fig. 3c). These results indicate EZH2 binds and methylate the AOX1 promoter, silencing AOX1 expression (Fig. 3d).

Knockdown of AOX1 altered cell morphology and increased cell proliferation, NADP levels, glucose metabolism, and nucleotide synthesis

To examine phenotypic responses to AOX1 modulation, we introduced AOX1shRNA or control shRNA constructs into SV-HUC-1 cells. Cells with AOX1 shRNA showed significant reduction in both AOX1 mRNA and protein (Fig.
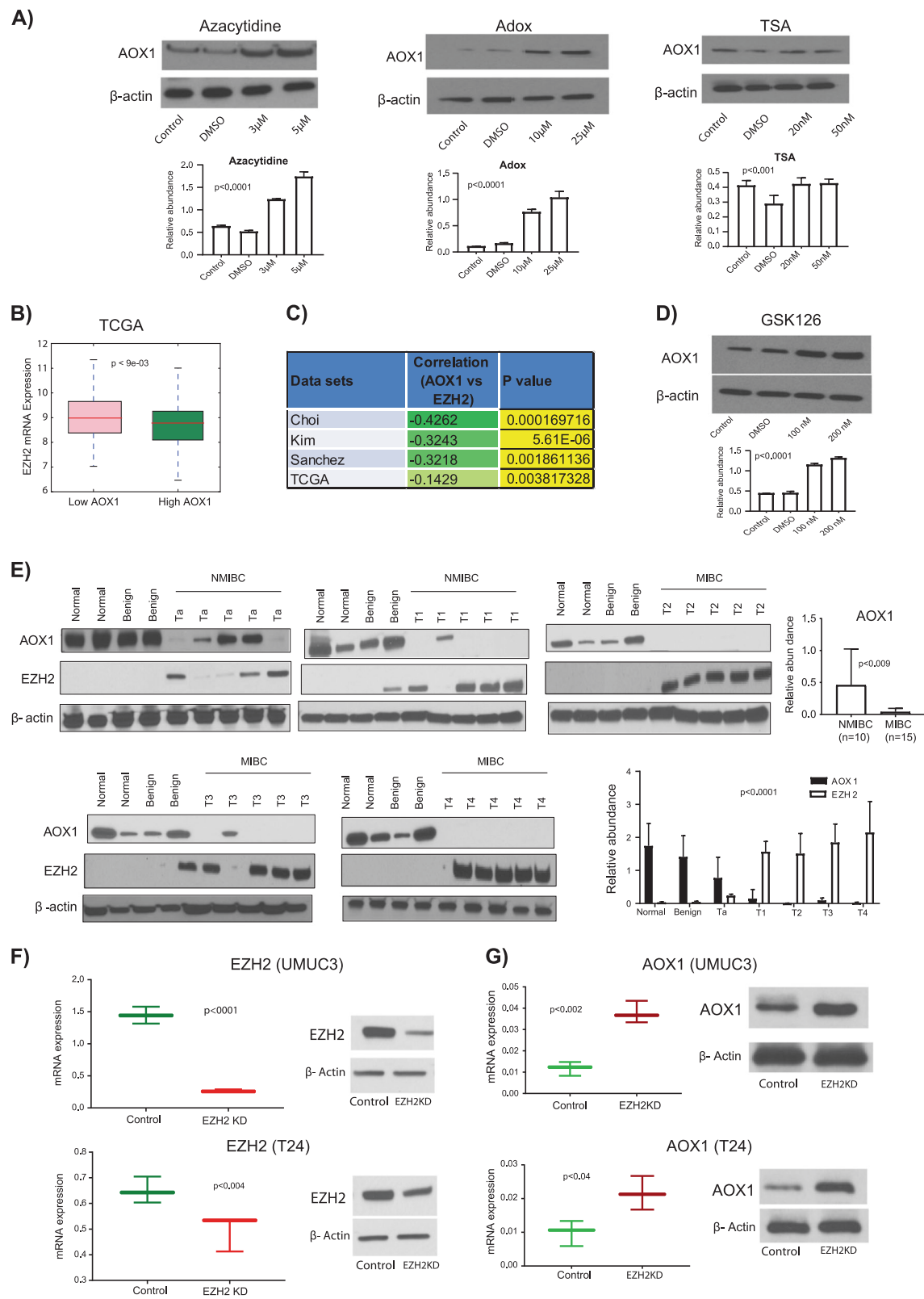
4a). AOX1 knockdown (KD) cells grew faster (Fig. 4b) and were significantly smaller (Fig. 4c) than control cells, showed altered cell growth and morphology. They also had

a significantly elevated growth rate compared with control cells (Fig. 4b). Cells were labeled with Alexa 594-conjugated phalloidin and the major and minor axis

◄ Fig. 2 EZH2-mediated suppression of AOX1 in BLCA. **a** Immunoblot analysis of AOX1 in UMUC3 cells treated with methylation and histone deacetylation inhibitors. Cells were treated with Azacitidine, Adox, and trichostatin A, respectively, for 24 h and the bar graphs show relative protein expression levels for the same blots. Protein levels were normalized using β-actin expression levels. **b** Negative correlation between AOX1 and EZH2 mRNA expression in TCGA. **c** Significant negative correlation ($p < 0.05$) between AOX1 and EZH2 mRNA expression in Choi, Kim, Sanchez, and TCGA cohorts. **d** Immunoblot analysis of AOX1 in UMUC3 cells treated with GSK126 for 24 h and the bar graphs show relative protein expression levels for the same blots. Protein levels were normalized using β-actin expression levels. **e** Immunoblot analysis of AOX1 and EZH2 at different stages of matched BLCA tissues and bar graphs show relative protein expression levels for the same blots. AOX1 quantification in NMIBC ($n = 10$) and MIBC ($n = 15$). Protein levels were normalized using β-actin expression levels. **f** qPCR and western blot of EZH2 shRNA knockdown in UMUC3 and T24. **g** qPCR and western blot of AOX1 in UMUC3 and T24 EZH2 knockdown cells. mRNA levels were normalized using GAPDH expression levels

lengths were calculated for each cell area. A significant decrease in cell size and major to minor axis length ratio was observed in AOX1 KD cells compared with control cells (Fig. 4c). A wound-healing assay to assess cell migration potential showed that the rate of wound closure was accelerated in AOX1 KD cells compared with control (Fig. 4d).

AOX1 is one of the key enzymes of tryptophan catabolism and loss of AOX1 may lead to the accumulation of kynurenine and NADP (Fig. 4e). To address this, we performed metabolomic analyses of AOX1 KD and control cells using liquid chromatography-mass spectrometry (LC-MS). AOX1 KD cells showed elevated levels of kynurenine, NADP, and a higher NADP/NADPH ratio compared with control cells (Fig. 4f). Isotropic tracing experiments with ^{15}N-labeled tryptophan demonstrated elevated levels of ^{15}N kynurenine in AOX1 KD cells (Fig. 4g) suggesting tryptophan may be shunted to the kynurenine pathway in the absence of AOX1.

We analyzed changes in the transcriptome in AOX1 KD cells by RNA sequencing and observed significant differences in levels of metabolic enzymes and epithelial-mesenchymal transition [23] markers (Fig. 4h). Metabolic flux analysis, using (U)[13]C glucose demonstrated, enrichment of glucose derived carbon in glucose-6-phosphate (M + 6), fructose 1,6-bisphosphate (M + 6), glyceraldehyde-3-phosphate (M + 3), and lactate (M + 3) in AOX1 KD compared with control (Fig. 4i). This suggested that the glycolytic pathway was activated in the absence of AOX1. PPP metabolites such as 6-phosphogluconate (M + 6), ribulose/xylose 5-phosphate (M + 5), and sedoheptulose 7-phosphate (M + 7) were also significantly increased in AOX1 KD compared with control (Fig. 4i). However, tricarboxylic acid (TCA) metabolites such as citrate (M + 2), succinate (M + 2), and malate (M + 2) showed lower incorporation of [13]C (Fig. 4i), which indicated reduced flow

of glucose into the TCA cycle in AOX1 KD. Nucleotide flux analysis showed a significant increase in the synthesis of adenosine monophosphate (M + 5), guanosine monophosphate (M + 5) cytidine monophosphate (M + 5), and inosine monophosphate (M + 5) in AOX1 KD (Fig. 4i). Immunoblotting assays showed elevated levels of the regulatory enzymes involved in glycolysis and PPP in AOX1 KD cells (Fig. 4j), which is consistent with the activation of glycolysis and PPP in cells without AOX1. Together, our results suggested that AOX1 played a critical role in regulating central metabolic pathways to divert glucose towards the PPP, which is a major source of intermediates for nucleotide synthesis in rapidly dividing cells.

Pharmacological inhibition of NAD synthesis rescued the metabolic effects caused by loss of AOX1

Because levels of kynurenine and NAD were elevated in the absence of AOX1, we tested whether pharmacological inhibition of NAD synthesis altered the metabolic effects caused by the loss of AOX1. NAD is predominantly synthesized via the kynurenine pathway and tryptophan 2,3-dioxygenase (TDO2) is the rate-limiting enzyme for this pathway [24]. AOX1 KD cells were treated with the TDO2 inhibitor, 680C91 [25], for 24 h. Levels of kynurenine, NAD, and PPP intermediates were measured by LC-MS (Fig. 4k). Inhibition of TDO2 resulted in decreased NAD synthesis leading to a reduction in 6-phosphogluconate and ribose/ribulose 5-phosphate in AOX1 KD cells compared with untreated AOX1 KD (Fig. 4k). These findings suggest loss of AOX1 in BLCA cells may enable increased NADP production.

Ectopic expression of AOX1 in BLCA cells affects NADP production, PPP metabolite levels, and nucleotide synthesis

To further assess the impact of AOX1 on central carbon metabolism, we ectopically expressed AOX1 in BLCA cells. UMUC3, and T24 cells were infected with adenovirus constructs expressing AOX1 (Ad-AOX1) and mRNA and protein levels were detected by western blotting and qPCR (Fig. 5a). Ectopic expression of AOX1 in BLCA cells significantly reduced the levels of kynurenine and NADP, suggesting activation of the regular tryptophan pathway (Fig. 5b). ^{15}N-labeled tryptophan flux also demonstrated decreased levels of ^{15}N kynurenine in Ad-AOX1 cells, confirmed the rewiring of the tryptophan-kynurenine pathway (Fig. 5c).

Next, we studied the effect of ectopic AOX1 expression on central carbon metabolism using U[13]C-labeled glucose in Ad-AOX1 UMUC3 BLCA cells. Ectopic AOX1 expression resulted in a decrease in levels of the glycolytic
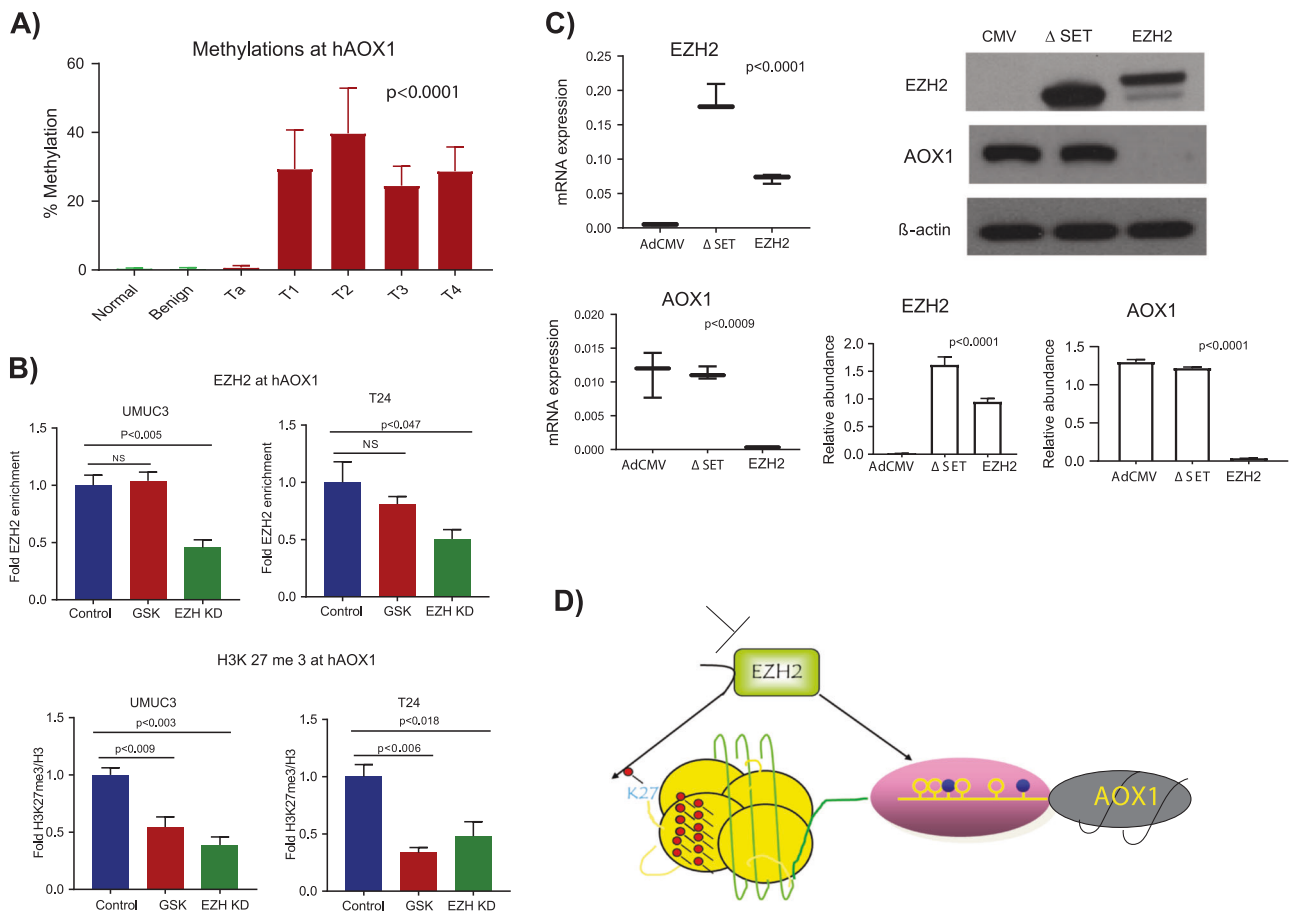
Fig. 3 EZH2-mediated hypermethylation at AOX1 promoter locus. **a** Quantification of DNA methylation using bisulfite repetitive PCR and pyrosequencing and percentage of DNA CpG methylation of the AOX1 promoter region at different stages of BLCA ($n = 4$, Normal, Benign Ta, T1, T2, T3, and T4). **b** qPCR analysis from ChIP shows significant reduction of the H3K27tri methylation at the AOX1 promoter in UMUC3 and T24 BLCA cell lines. 100 nM GSK126 reduces the H3K27 trimethylation at AOX1 promoter without affecting EZH2 levels. On the other hand, EZH2 knockdown significantly affected EZH2 occupancy and H3K27 trimethylation at the AOX1 promoter locus. EZH2 enrichment is normalized to IgG and H3K4me3/K27me3 markers are normalized to IgG and H3. **c** mRNA analysis and immunoblots of SV-HUC-1 cells infected with adenovirus encoding EZH2 or Δ SET mutant and vector adenoviruse for 48 h. Ectopic overexpression of EZH2 significantly reduces AOX1 expression but ΔSET mutant does not have effect on AOX1 expression, the bar graphs show relative protein expression levels for the same blots. Protein levels were normalized using β-actin expression levels. **d** Graphical representation of AOX1 suppression by EZH2-mediated promoter methylation

intermediates, glucose-6-phosphate (M + 6) and fructose 1,6-bisphosphate (M + 6) (Fig. 5d). However, levels of the TCA cycle intermediates, citrate (M + 2), succinate (M + 2), and malate (M + 2), were elevated (Fig. 5d), suggesting a shift in carbon metabolism toward the TCA cycle. Accordingly, levels of PPP intermediates, 6-phosphogluconate (M + 6), ribulose/xylose 5- phosphate (M + 5), and sedoheptulose 7-phosphate (M + 7) were decreased in Ad-AOX1 BLCA cells (Fig. 5d). Analysis of nucleotide flux in Ad-AOX1 BLCA cells showed decreased levels of adenosine monophosphate (M + 5), guanosine monophosphate (M + 5), cytidine monophosphate (M + 5), and inosine monophosphate (M + 5) (Fig. 5d).

To further examine the role of AOX1 in metabolic regulation of tryptophan and PPP pathways in BLCA, we compared the effect of gain and loss-of-function of AOX1 in the UMUC3 cells. UMUC3 does not natively express meaningful amounts of AOX1. Therefore, UMUC3 cells were maintain in a sublethal dose of GSK126 until AOX1 expression was achieved (Fig. 5e). The enzymatic activity of AOX1 was active in GSK126-treated cells as evidenced by low levels of kynuerenine, NADP and PPP pathway metabolites (Fig. 5f). In contrast, the knockdown of AOX1 under these conditions significantly increases the abundance of kynuerenine, NADP and PPP pathway metabolites (Fig. 5f), further corroborating the role of AOX1 in metabolic rewiring of tryptophan towards increased NADP synthesis. Together, these experiments suggest AOX1 plays a pivotal role in central carbon metabolism by rewiring the tryptophan metabolic pathway, which further regulates PPP pathway through NADP.
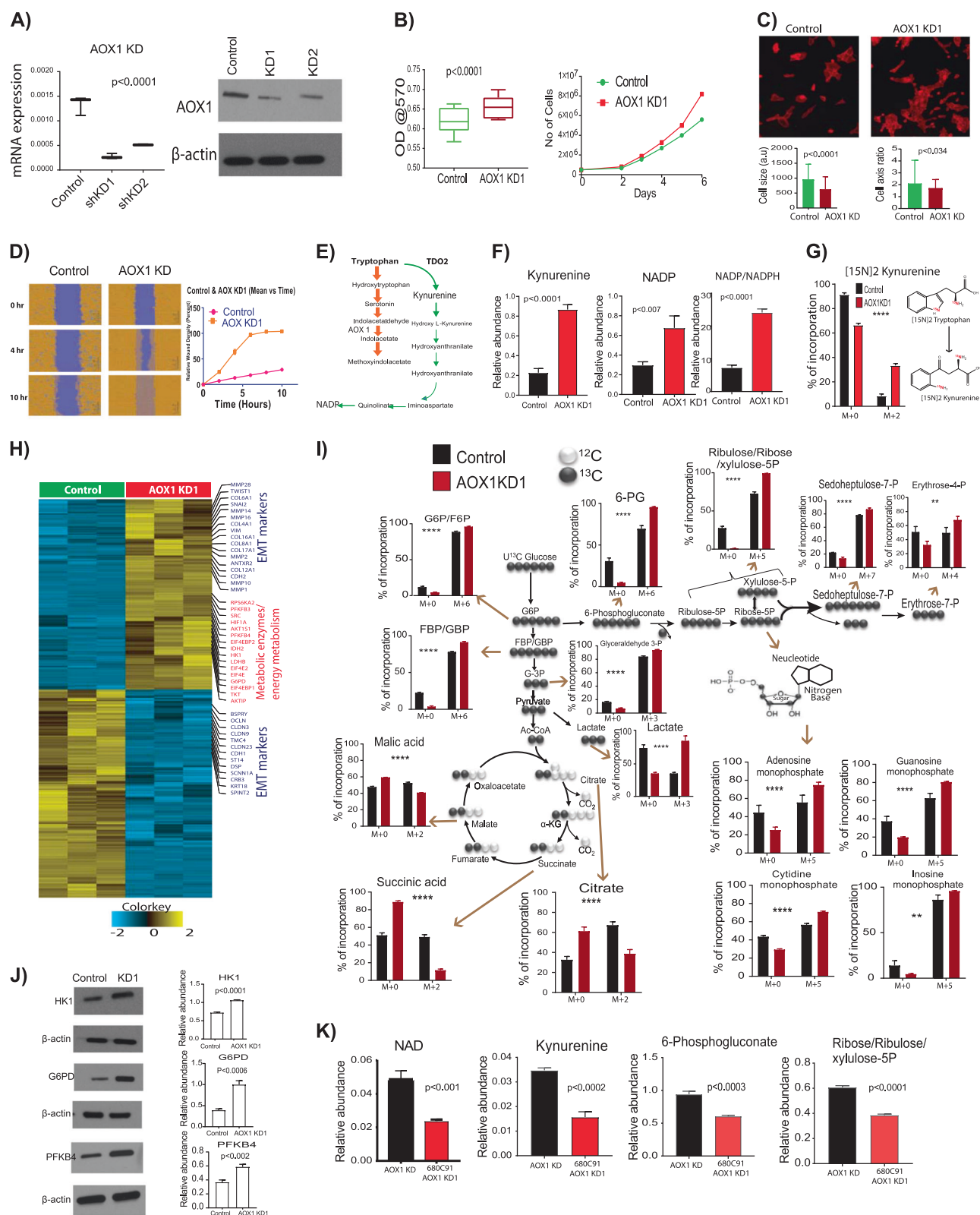
Fig. 4 Knockdown of AOX1 altered cell morphology and increased cell proliferation, glucose metabolism, and nucleotide synthesis. **a** shRNA knockdown (KD) of AOX1 in SV-HUC-1 leads to significant reduction in mRNA and protein levels. **b** Cell viability and proliferation of AOX1 KD cells. The cytotoxicity was determined by MTT assay. For proliferation assay 0.5×10^6 vector control and AOX1 KD cells were cultured in 100-mm culture dishes in triplicate. Total cells were counted on days 2, 3, 4, 5, and 6 using a Countess automated cell counter. **c** AOX1 KD causes the reduced cell size. Cell size and the ratio between the major axis length and the minor axis length were compared between control ($n = 76$) and AOX1 KD ($n = 159$) cells. **d** Wound-healing assay shows high migration rate of AOX1 KD cells compared to control. AOX1 KD and vector control cells were plated in 96-well image lock plate and grown to full confluency. Scratch was made using IncuCyte wound maker. The images were captured every 2 hours using Incucyte ZOOM. The images were analyzed for relative wound density (%) on Integrated cell migration analysis module. **e** Tryptophan-kynurenine pathway for the synthesis of NADP. **f** Kynurenine, NADP, and NADP/NADPH ratio levels in control and AOX1 KD measured by LC-MS. Metabolite levels were normalized using ^{13}C labeled internal standards to represent relative abundance level. **g** ^{15}N tryptophan flux shows elevated levels of ^{15}N kynurenine (M + 2) in AOX1 KD1 compared to control. **h** Heat map showing differential ($P < 0.05$) genes in AOX1 KD compared with vector control. **i** ^{13}C-labeled metabolic flux results in elevated levels of glycolytic intermediates, glucose-6-phosphate (M + 6) and fructose 1, 6-bisphosphate (FBP) (M + 6); increased levels of PPP intermediates, ribulose 5-phosphate (M + 5), sedoheptulose 7-phosphate (M + 7), and erythrose 4-phosphate (M + 4); increased levels of nucleotides, AMP, GMP, CMP, and IMP; decreased levels of TCA intermediates, citrate (M + 2), succinate (M + 2), and malate (M + 2) in AOX1 KD. **j** Western blot analyses for HK1, G6PD, and PFKB4 expression in AOX1 KD cells and the bar graphs show relative protein expression levels for the same blots. Protein levels were normalized using β-actin expression levels. **k** NADP, kynurenine, 6PG, and ribose/ribulose 5-P relative measurements by LC-MS analysis. M + 2, M + 5, M + 6, and M + 7 indicate two, five six, and seven Dalton shift respectively compare to unlabeled metabolites

Loss of AOX1 induces EMT phenotype and invasion in BLCA

EMT is a crucial mechanism by which cancer cells gain migratory and invasive properties [26, 27]. Our results demonstrate SV-HUC-1 AOX1 KD cells display altered cell growth, morphology, and metabolic phenotype. To further examine the link between AOX1 and EMT, we measured mRNA and protein expression levels of EMT markers such as E-cadherin, vimentin, and N-cadherin in AOX1 KD and Ad-AOX1 cells. AOX1KD cells showed lower levels of E-cadherin and higher levels of vimentin and N-cadherin (Fig. 6a). In contrast, Ad-AOX1 BLCA cells showed increased expression of E-cadherin and decreased expression of vimentin (Fig. 6b). Therefore, loss of AOX1 during BLCA progression may contribute to the EMT phenotype of cancer cells. Cell invasion assays showed loss of AOX1 resulted in increased invasiveness of SV-HUC-1 cells (Fig. 6c) and Ad-AOX1 decreased invasiveness of high-grade UMUC3 and T24 BLCA cells (Fig. 6d). These results suggest loss of

AOX1 contributes the transition from low-grade to high-grade during BLCA progression.

AOX1 suppresses the tumor potential of BLCA cells in vivo

To examine the tumor-suppressive potential of AOX1 in vivo, we introduced Ad-AOX1 into UMUC3 BLCA cells, which were then injected into the flank region of immunocompromised mice. UMUC3 BLCA cells with empty adenoviral vectors were used as control. Tumors were collected for analysis after 4 weeks of growth. We found that tumors of Ad-AOX1 showed significantly reduced growth rate and size compared with control tumors (Fig. 7a, b). To determine whether AOX1 regulated the same biochemical pathways in vitro and in vivo, we analyzed AOX1-associated metabolites and nucleotides by LC-MS. We found that the Ad-AOX1 tumors were enriched in energy metabolites and AOX1-product metabolites, and showed lower levels of nucleotides and AOX1-substrate metabolites (Fig. 7c). To further examine the role of AOX1 in tumor growth, we performed chicken embryo chorioallantoic membrane [5] xenografts [28] to assess the effects of gain and loss-of-function of AOX1. GSK126 treated cells were used for AOX1 gain, followed by shAOX1 knockdown for loss of AOX1 in the same setting. One million cells from each experimental group (control, GSK, GSK + luc, and GSK + shAOX1) were grafted on the embryo's CAM and allowed to expand for 5 days. We found AOX1 expression resulted in a significant reduction in tumor growth while AOX1 knockdown enhanced growth (Fig. 7d). Immunohistochemistry (IHC) analysis of the CAM tumors demonstrated the expected experimental loss and gain of AOX1 (Fig. 7d). In addition, we have performed EZH2 overexpression followed by AOX1 overexpression in cell line model (Supplementary Fig. 6a). The results demonstrated reduced tryptophan pathway metabolites, NADP, and PPP intermediates (Supplementary Fig. 6b) and increase in ovivo tumor growth (Supplementary Fig. 6c). Overall these results indicate expression of AOX1 reduces nucleotide synthesis and suppresses tumor growth in vivo.

Discussion

Previous metabolomic studies have investigated disease-specific metabolite signatures in BLCA [9, 29, 30]. Our study is the first to identify stage-specific metabolic markers associated with AOX1 that are predictive of BLCA progression. We found the metabolic state of bladder tumors at the Ta stage was markedly different from that of tumors at the T1–T4 stages. The accumulation of AOX1-substrate
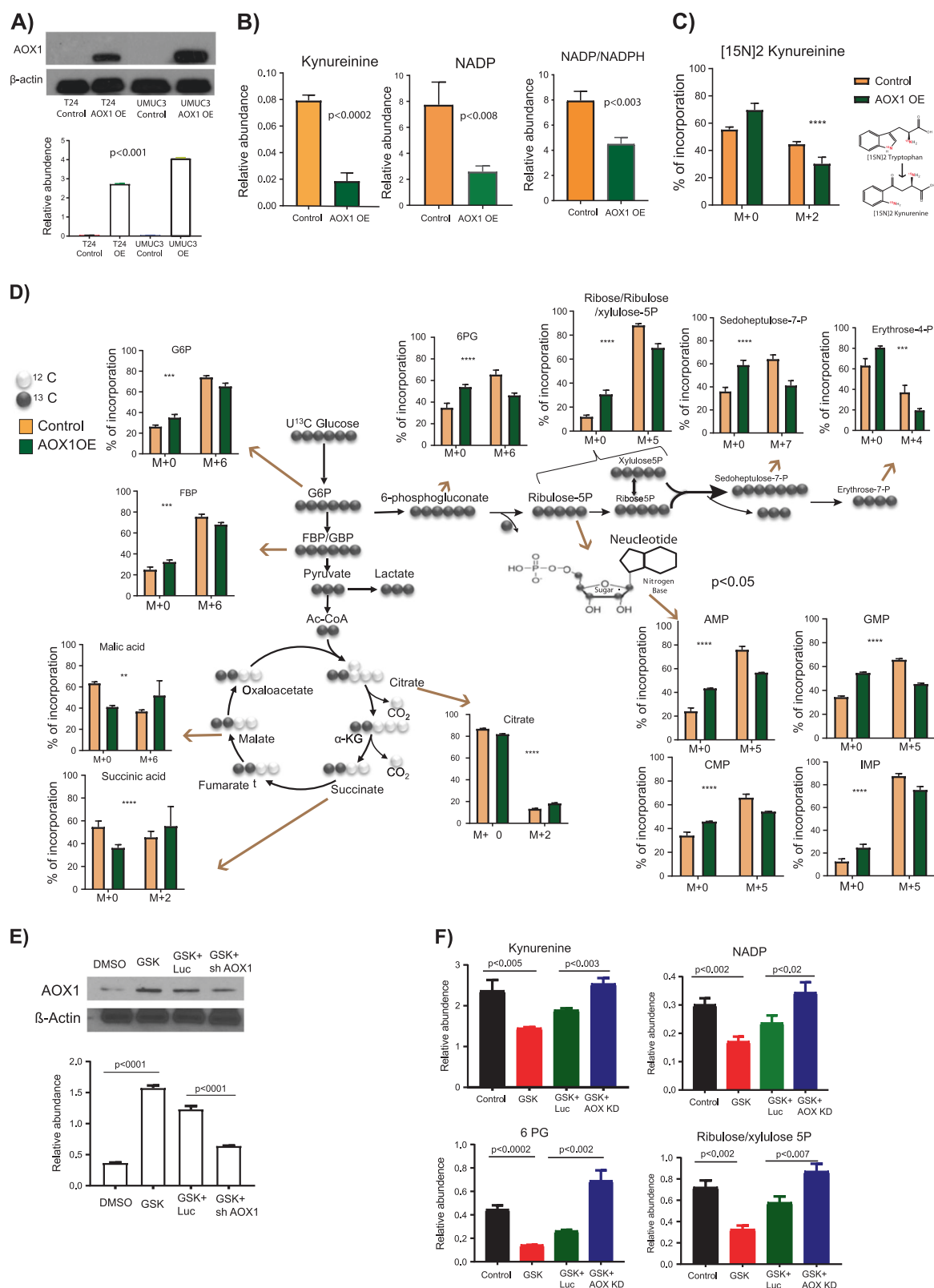
metabolites, such as tryptophan, tyrosine, retinol, nicotinamide, and indole acetaldehyde and the reduction of AOX1-product metabolites, such as gentisate, retinoic acid, indole acetate, and TCA metabolites in advanced BLCA tissues suggests AOX1 loss is an indicator of high-grade BLCA. Previous studies have shown that some of these metabolites

◄ **Fig. 5** Ectopic expression of AOX1 in BLCA affects NAD/NADP, pentose phosphate pathway, and nucleotide synthesis. **a** Adenoviral ectopic expression (Ad-AOX1) of AOX1 in UMUC3 and T24 cells causes upregulation of AOX1 protein levels. **b** Levels of kynurenine, NADP, and NADP/NADPH ratio in control and Ad-AOX1 UMUC3 cells. Metabolite levels were normalized using internal standards to represent relative abundance level. **c** ^{15}N tryptophan flux shows decreased levels of ^{15}N kynurenine $(M + 2)$ in Ad-AOX1 UMUC3 cells compared with control. **d** ^{13}C-labeled metabolic flux results of Ad-AOX1 UMUC3 cells shows decreased levels of glycolytic intermediates, glucose-6-phosphate $(M + 6)$, fructose 1, 6-bisphosphate $(M + 6)$; decreased levels of PPP intermediates, ribulose 5-phosphate $(M + 5)$, sedoheptulose 7-phosphate $(M + 7)$, and erythrose 4-phosphate $(M + 4)$; decreased nucleotides, AMP, GMP, CMP, and IMP; and elevated levels of TCA intermediates, citrate $(M + 2)$, succinate $(M + 2)$, and malate $(M + 2)$. $M + 2$, $M + 5$, $M + 6$, and $M + 7$ indicate two, five six, and seven Dalton shift respectively compare to unlabeled metabolites. **e** Western blot analysis AOX1 gain and loss upon 100 nM GSK treatment followed by shAOX1. Protein levels were normalized using β-actin expression levels for the quantification. **f** Levels of kynurenine, NADP, 6-phosphogluconate and ribulose/xylulose-5-phosphate during AOX1 gain and loss conditions. Metabolite levels were normalized using internal standards to represent relative abundance level

play a significant role in the development of various cancers [31–35]. It is possible that some of these metabolites play a crucial role in the clinical outcome of the BLCA and thus may be useful prognostic markers for BLCA. Our study also found high-grade BLCA tumors showed low levels of AOX1 expression, thus, highlighting the possible prognostic potential of AOX1 in BLCA. Recent studies have shown that AOX1 expression is low in breast, prostate, colorectal, and ovarian cancers [23, 36–38], but the metabolic significance of AOX1 levels in these cancers remains unknown. Our study has identified the predictive power of AOX1 associated metabolites for BLCA prognosis. However, the practical clinical implications of these prognostic markers for BLCA need to be further elucidated.

EZH2 is an epigenetic modulator that is commonly expressed at high levels in many types of cancers, such as melanoma, glioblastoma, breast, prostate, endometrial, liver, and lung [39–43]. We found that EZH2 expression was up-regulated in aggressive BLCA compared with benign and Ta stage tumors. This result supports a recent study demonstrating loss of tumor suppressor KDM6A (a H3K27 demethylase) amplifies PRC2-regulated transcriptional repression by EZH2 in BLCA [42]. GSK126 [44], treatment leads to reactivation of AOX1 by inhibiting EZH2, which suggests that small molecule drugs that target epigenetic enzymes provide a promising target to develop effective therapeutic agents against advanced BLCA. The EZH2 small molecule inhibitors Tazemetostat, EPZ005687, GSK343, UNC1999, and EPZ-6438 are in clinical trials to treat various advanced cancers [45, 46] ChIP experiments, and SET domain studies also demonstrated that the methyltransferase activity of EZH2 was essential for

H3K27 methylation at AOX1 promoter. Our results add merit to the emerging mechanisms of epigenetic gene silencing of xenobiotic enzymes during BLCA development. Hypermethylated genes have been shown to be promising cancer markers for early detection of BLCA [47, 48]. DNA hypermethylation is a common mechanism to silence many tumor suppressor genes [48, 49]. Muscle invasive bladder cancer (MIBC) shows distinct patterns of CpG island hypermethylation at the AOX1 promoter when compared with NMIBC [49]. Hyper DNA methylation of AOX1 promoter in advanced stage BLCA patients and AOX1 negative correlation of AOX1 with DNMT3b in public cohorts also suggests the occupied EZH2 at AOX1 promoter may be interacts with DNMT3b and associated with it DNA methyltransferase activity in vivo [21].

NAD and NADP are required for various biological processes, including energy metabolism, oxidative stress, immunological functions, aging, and cell death [50, 51]. NAD/NADP is produced through the tryptophan- kynurenine pathway by the rate-limiting enzyme Tryptophan 2,3-dioxygenase (TDO2). Loss of AOX1 may disrupt the tryptophan- kynurenine pathway resulting in production of NADP and fueling nucleotide synthesis. We also demonstrated a significant effect on invasion in AOX1 KD and Ad-AOX1 BLCA cells. It is possible that the effects could be mediated through either the tryptophan-kynurenine pathway intermediates or via NAD/NADP. Kynurenine is an important intermediate of this pathway and can act as an important signaling molecule. Kynurenine may mitigate immune suppressive effects by binding to the aryl hydrocarbon (AhR) receptor there by promoting invasion and metastasis [52]. NAD also acts as a cofactor for many enzymes particularly sirtuins, which regulate many cellular pathways involved in cell invasion and metastasis [53, 54].

Loss of AOX1 leads to upregulation of metabolic enzymes such as hexokinase 1, phosphofructokinase 1, and glucose-6-phosphate dehydrogenase, which suggest a possible role for increased glucose metabolism in activating the PPP. Ribose 5-phosphate, a major product of the PPP is the precursor for nucleotide and nucleic acid synthesis [55]. Signaling events that promote flux through PPP could enhance tumor growth by fueling nucleotide synthesis. Our results suggest, TDO2 is an important contributor to NADP synthesis through kynurenine production in AOX1 BLCA. TDO2 expression is increased in metastatic uterine leiomyosarcoma and glioma [56, 57]. Moreover, increased levels of kynurenine is associated with breast cancer metastasis to lung and brain [58, 59]. The effects of gain and loss-of-function of AOX1 demonstrated that AOX1 plays an essential role in regulating tryptophan pathway by modulating NADP production and there by the PPP pathway. Thus, multiple metabolic pathways may be altered to provide the necessary precursors for rapidly proliferating
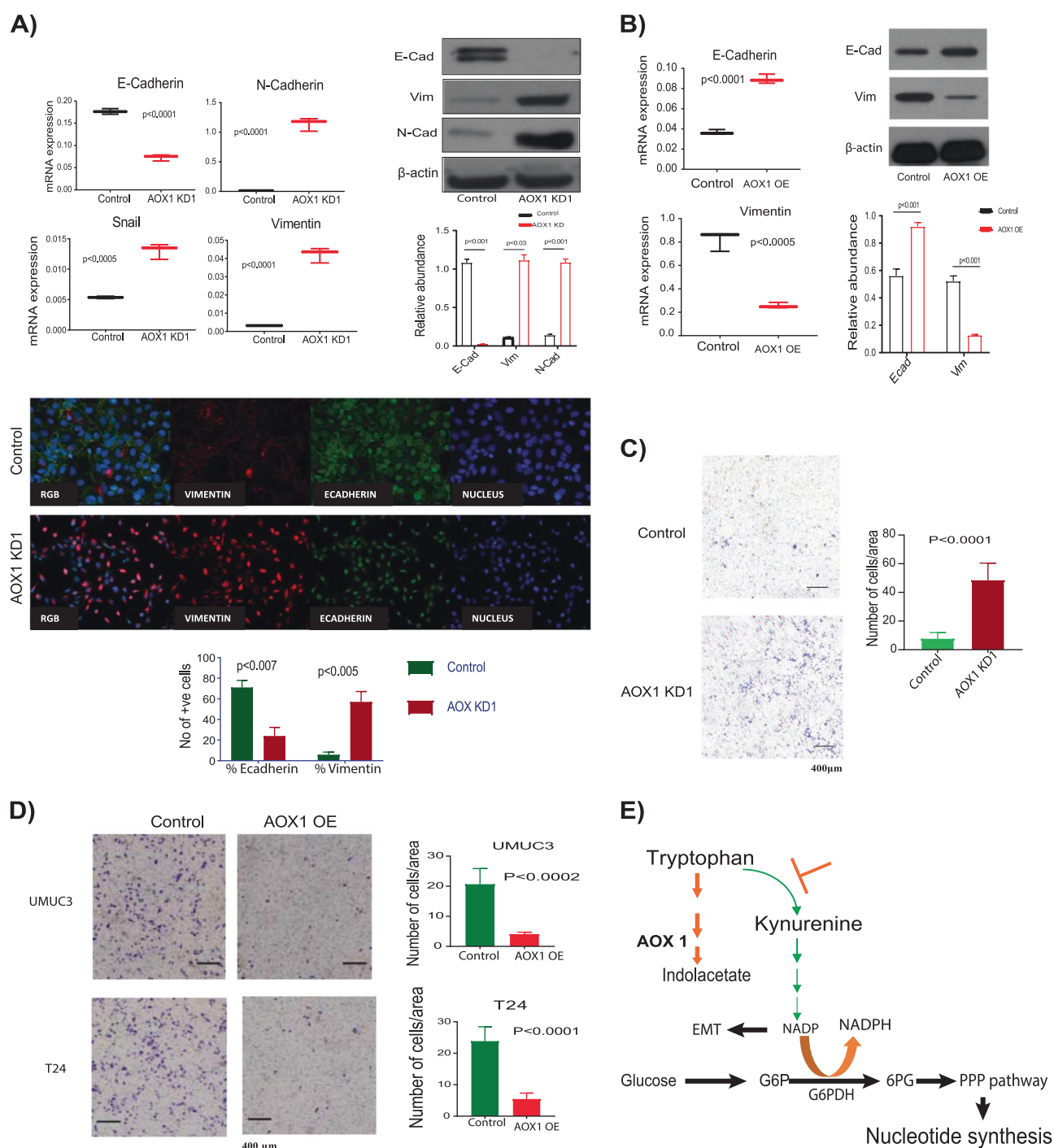
Fig. 6 Loss of AOX1 triggers EMT phenotype and invasion in BLCA. **a** mRNA and protein expression of EMT markers (E-cadherin, N-cadherin, and Vimentin) in AOX1 KD cells and their quantification. β-actin was used as internal control. Immunofluorescence microscopy of E-cadherin and vimentin expression in AOX1 KD and control cells. **b** Ad-AOX1 in UMUC3 shows increased levels of E- cadherin and decreased vimentin. **c** Boyden chamber cell invasion assay of AOX1 KD shows the increased invasion. **d** Boyden chamber cell invasion assay of Ad-AOX1 in UMUC3 and T24 cells, shows reduced cell invasion after 48 hours incubation. Cells were stained with crystal violet, counted in five individual fields, and the mean values were determined. **e** Graphical representation of rewired tryptophan-kynurenine pathway in AOX1 KD that leads to metabolic activation of PPP and nucleotide synthesis

cells during tumor progression. Pharmacologic inhibition of TDO2 in AOX1KD decreases flux through PPP suggesting

a novel therapeutic opportunity to suppress nucleotide biosynthesis at the level of the kynurenine pathway.
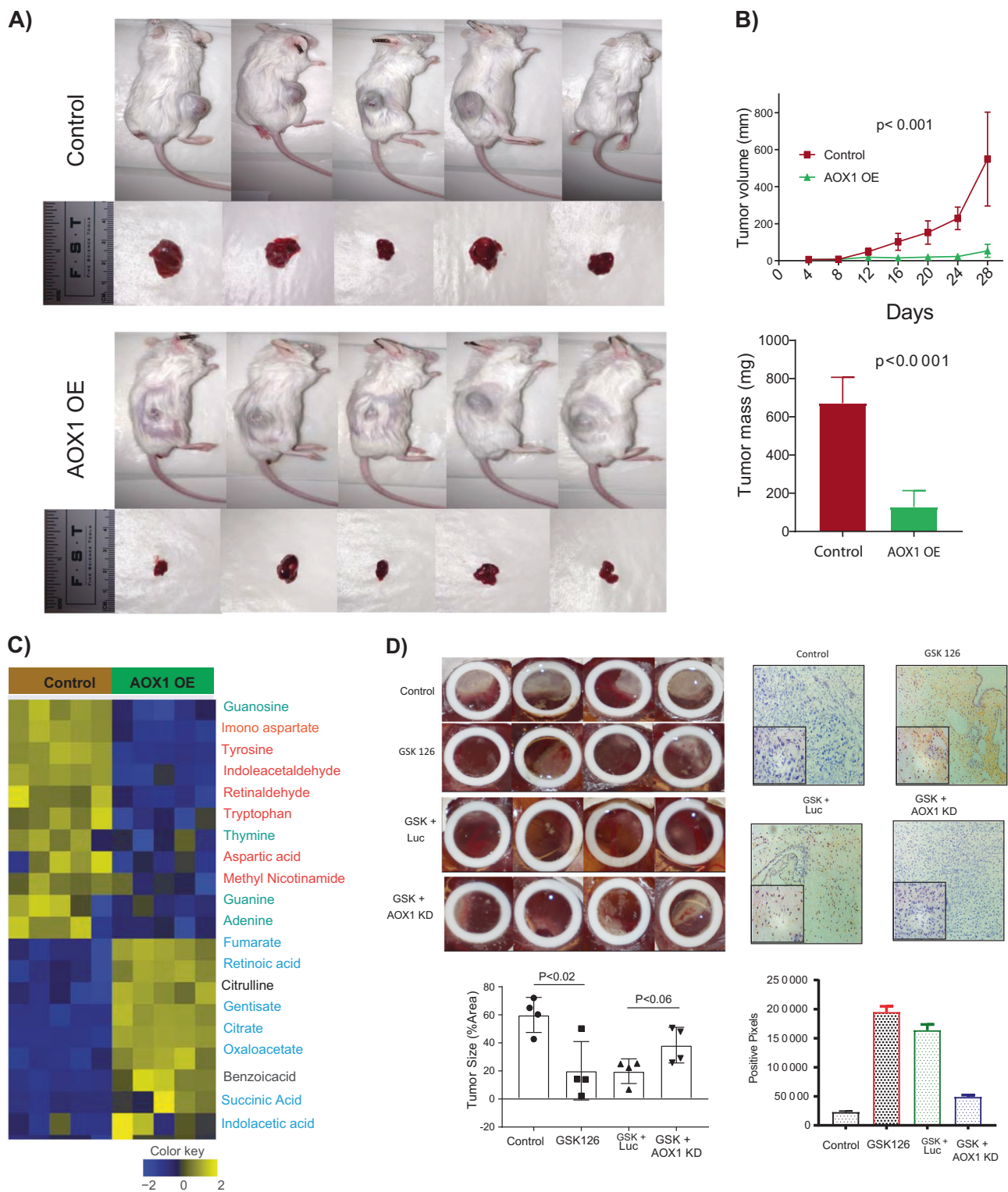
In conclusion, we show that loss of AOX1 expression in BLCA is mediated by the methyltransferase activity of EZH2. This leads to rewiring of the tryptophan-kynurenine pathway resulting in elevated NADP levels that potentially drive carbon flux through the PPP and promote EMT and cell invasion during BLCA progression. This is the first study to demonstrate the generation of NAD/NADP via a previously unrecognized pathway in response to loss of

Fig. 7 AOX1 Suppresses in vivo tumor potential of BLCA cells. **a** Mice xenograft shows reduced tumor size upon ectopic expression of Ad-AOX1 in UMUC3 BLCA cells. **b** UMUC3 xenograft tumors containing Ad-AOX1 show a significantly lower growth rate compared with controls ($n = 5$, Ad-h-AOX1 and $n = 5$ vector control). Y-axis represents median tumor volumes in mm^3 and associated median absolute deviation (MAD) for each group and Tumor mass after 28 days. **c** Heat map of hierarchical clustering of differential metabolites in tumor xenograft after 28 days. Shades of yellow and blue represent higher and lower levels of metabolites, relative to the median metabolite levels, respectively (false discovery rate, FDR < 0.25). **d** The CAM assay for the AOX1 gain and loss conditions after 5 days. To gain the AOX1 UMUC3 cells continuously treated with 100 nM GSK in CAM. Tumor size on the CAM was calculated as a percentage of the total area within the inner, 9 mm portion of the silicon ring. ImageJ was used to manually segment the area occupied by each of the tumors in all groups. IHC of CAM tissues confirm the gain and loss of AOX1 and stained slides were scanned using Aperio CS2 and analyzed with Aperio positive pixel count algorithm for quantification

AOX1, thus connecting metabolism and carcinogenesis. Furthermore, our stage-specific metabolomic data provide a basis for prognostic and therapeutic measures for advanced BLCA. Future studies should focus on in-depth analyses of AOX1 regulation and function to help identify effective prognostic and therapeutic targets for BLCA.

Materials and methods

Reagents

Acetonitrile, methanol, and water for high-performance liquid chromatography were purchased from Burdick and Jackson. Formic acid and internal standards, Gibberellic acid, Jasmonic acid, [^{15}N]2-Tryptophan, Thymine-d4, [^{13}C]-Creatinine, [^{15}N] Arginine, [^{15}N]-Anthranilic acid, and Testosterone-d3 (Supplementary Table 3), were purchased from Sigma Aldrich. U^{13}6 glucose was used purchased from Cambridge isotope laboratories, 5-Azacytidine, Adox, 680C91 were purchased from Sigma and GSK126 was procured from Cayman chemicals.

Tissue microarray

Tissue Microarray [3] slide with all the BLCA stages was procured from US Biomax. Immunostaining was performed using AOX1 antibody (Proteintech, 1:100 dilution) and AOX1 expression was analyzed and scored by a genitourinary pathologist. The scores of 0–3 were considered low and scores from 4–8 were considered high. The score represents a combination of staining intensity and percentage of tumor cells showing protein expression

Cell culture, generation of stable AOX1, EZH2 knockdown, and Ad-h-AOX1 in BLCA cells

SV-HUC-1, RT4, T24, UMUC3 J82, and TCCSUP were procured from American Type Culture Collection (ATCC) and maintained as per ATCC instructions. All cell lines were verified using Short-Tandem Repeat DNA fingerprinting at the MD Anderson Cancer Center and were tested negative for mycoplasma contamination using MycoAlert Detection Kit (Lonza). To generate stable AOX1 and EZH2 KD in SV-HUC-1, UMUC3, and T24 cells, lentiviral transduction using shRNA (Sigma Aldrich) was carried out at a viral titer of 5 MOI. Cells with stable KD of the gene were cultured in respective media with 1 μg/ml of puromycin. Knockdown was assessed by qRT-PCR and western blotting. Customized Ad-h-AOX1 was procured from vector bio labs and transfections carried out according to manufacturer's instructions.

Targeted metabolomics using mass spectrometry

Human tissue samples were stored at −140 °C until the analysis. All the BLCA specimens were procured from UTSW (The University of Texas Southwestern Medical Center), UWH (Witten-Herdecke University), and BCM (Baylor College of Medicine) according to a prior written informed consent under institute review board (IRB) approved protocols Mice experiments were conducted according to the guidelines for humane treatment of animals approved by Baylor College of Medicine. For validation studies, we used an aliquot of extracted samples from earlier studies [60, 61].

Sample preparation for mass spectrometric analysis

Metabolites were extracted from tissues, cell lines, following the extraction procedure described previously [9, 62–65] and and mouse liver pool was used as quality controls. For metabolomics, 25 mg of tissue homogenized in ice cold water: methanol (1:4) containing an internal standards (Supplementary Table 3). For cell lines, 3×10^6 cells were subjected to three freeze-thaw cycles in liquid nitrogen and ice alternatively for three times to rupture the cell membrane. Following this, cells were sonicated in ice cold water: methanol (1:4) containing an internal standards (Supplementary Table 3). This was followed by metabolic extraction using sequential application of ice cold organic and aqueous solvents methanol: chloroform: water 4:3:2), deproteinization and drying of the extract. The latter was resuspended in injection solvent, and 5 μl used for LC-MS. LC-MS performed on Agilent 1290 series HPLC system

equipped with a degasser, binary pump, thermostatted autosampler and column oven. The multiple reaction monitoring (MRM)-based measurement of relative metabolite levels (Supplementary Table 5), used either reverse phase or normal phase chromatographic separation.

Separation of metabolites

Electrospray ionization (ESI) Positive mode was used to separate the metabolites. The LC column was Waters XBridge Amide 3.5 μm, 4.6 × 100 mm. Mobile phase A and B were 0.1% formic acid in water and acetonitrile respectively. Gradient: 0 min-85% B; 3–12 min- 85% to 10% B, 12–15 min-10% B, 16 min- 85% -B, followed by re-equilibration end of the gradient- the 23 min to the initial starting condition 85% B. Flow rate: 0.3 ml/min. ESI negative mode was also used to separate the metabolites. The HPLC column was Waters XBridge Amide 3.5 μm, 4.6 × 100 mm. Mobile phase A and B were 20 mM ammonium acetate in water with pH 9.0 and 100% acetonitrile respectively. Gradient: 0 min-85% B; 0–3 min- 85% to 30% B, 3–12 min-30%-2% B, 12–15 min- 2% -B, 15–16 min- 85% B followed by re-equilibration end of the gradient- the 23rd min to the initial starting condition 85% B. Flow rate: 0.3 ml/min.

Statistical analysis

The data was log2 transformed and normalized with internal standards on a per-sample, per-method basis. For every metabolite in the normalized dataset, two sample t-tests were conducted to compare expression levels between Ta and other stages (T1–T4). Differential metabolites were identified by adjusting the p-values for multiple testing at an FDR threshold of <0.25. A hierarchical cluster of the differentially expressed metabolites was generated using the R statistical software system (https://www.r-project.org/).

Generation of the ROC plots

We used 119 tissue specimens collected at three institutions (clinical information in Supplementary Table 2) and selected a subset of seven metabolites such as Nicotinamide, Methyl adenosine, Asparagine, Methyl histidine, Indolacetaldehyde, Tyrosine, Gentisatealdehyde which are associated with AOX1 metabolic pathways to derive an activity score. The metabolic data was normalized following median IQR and log2 transformed prior to running the predictive analyses. The dataset was z-score transformed. These subset of seven metabolites was used to estimate an overall activity score for each sample. For each individual sample, out of those seven metabolites, the total sum of negative z-scores was calculated and subtracted from total sum of positive z-scores (measured in a similar manner from remaining

metabolites out of seven) to yield the final activity score for that sample. Next, using the activity scores as an input, we implemented a logistic regression model to build a predictive classifier on the disease status.

Following the method described above, we build a training model using the activity scores derived from two-thirds of the samples (selected randomly, $n = 80$). Next, we validated the predictive performance of the classifier by employing it on a test dataset comprised of remaining one-third of the samples ($n = 39$). Again the activity scores of the test samples were the input for the previously built model and the goal was to test if using those activity scores, it can predict the actual status (disease vs. control) in the test dataset. The classifier performance was characterized by measuring the area under Receiver Operating Characteristic (ROC) curve. The AUC value was 0.689 with a significance level of $p = 0.023$.

Pathway analysis

Networks of all pathways were visualized using the Fruchterman-Reingold layout algorithm implemented in the R package 'igraph'. Each node represents a metabolic pathway, with node sizes indicating statistical significance ($-\log10$(adjusted p-value) - larger nodes correspond to lower p-values). An edge is drawn between two pathways if they have one or more metabolites in common. The width of an edge indicates the number of common metabolites between two pathways.

Promoter methylation analysis by bisulfite sequencing

The promoter methylation by bisulfite sequencing protocol used in this study was described earlier [66]. In brief, genomic DNA isolated from tissues by DNeasy blood and tissue kit (Qiagen). In all, 600 ng of genomic DNA from was treated with sodium bisulfite using the EZ DNA Methylation-Gold Kit (Zymo Research) according to the manufacturer's protocol. The samples were eluted in 40 μl of M-Elution Buffer, and 2 μl (equivalent to 25 ng of bisulfite-modified DNA) were used for each PCR reaction. Both bisulfite conversion and subsequent pyrosequencing analysis were done at the DNA Methylation Analysis Core, The University of Texas MD Anderson Cancer Center. PCR primers for the genomic area proximal to the transcription start site (TSS) of AOX1 (interrogating six CpG sites between 1-bp and 27-bp from TSS) were designed using the Pyromark® Assay Design SW 2.0 software (Qiagen). A sequencing primer is identified within 1–5 base pairs near the CpG sites of interest, with an annealing temperature of $40 \pm 5\,^{\circ}C$. After that, forward and reverse primers are identified upstream and downstream to the sequencing

primer, with a target annealing temperature ranging from 50 °C to 60 °C and amplicon product size ranging from 100 to 200 bp. Controls for high methylation (SssI-treated DNA), low methylation (WGA amplified DNA), and no-DNA template were included in the PCR reaction. PCR product purification was done with streptavidin-sepharose high-performance beads (GE Healthcare Life Sciences), and co-denaturation of the biotinylated PCR products and sequencing was conducted following the PSQ96 sample preparation guide. Sequencing was performed on a Pyro-Mark Q96 ID instrument with the PyroMark Gold Q96 Reagents according to the manufacturer's instructions. The degree of methylation for each individual CpG site was calculated using the PyroMark Q96 software (Biotage AB). The average methylation of all sites and duplicates was reported for each sample.

Chromatin immunoprecipitation

ChIP assays were performed using a high throughput protocol as described [67]. In brief, cells were crosslinked in 1% formaldehyde for 10 min at room temperature, followed by incubation with glycine for 5 min to stop crosslinking. Cells were collected and washed with ice cold PBS and lysed for 30 min on ice using lysis buffer (12 mM Tris-HCl pH 7.5, 6 mM EDTA pH 8.0, 0.5% SDS) supplemented with a protease inhibitor. Lysates were fragmented with a Bioruptor (Diagenode) to obtain DNA fragments ranging 200–600 bp. After centrifugation, the supernatant was collected and incubated with respective antibodies conjugated with Dynabeads Protein G (Invitrogen) overnight at 4 °C. The immunocomplexes were collected using Dynamag, washed as described in the protocol, treated with RNase and Proteinase K, and reverse crosslinked overnight followed by DNA extraction. The DNA region of interest was detected by SYBR green real-time quantitative PCR using primer encompassing EZH2 binding and H3K4me3/H3M27me3 enrichment locus on human *AOX1* promoter determined using ENCODE database. The sequences of the forward and reverse primers used for ChIP-qPCR at *AOX* promoter are described in Supplementary Table 4.

Boyden Chamber invasion assay

Cell migration and invasion were measured using trans well chambers (Corning, USA) according to the manufacturer's protocol. AOX1 KD and Ad-AOX1 UMUC3 and T24 cells were incubated for 48 hours. Then, the cells in the upper chamber were removed with sterile cotton buds, and the remaining cells were fixed in 4% paraformaldehyde and stained with crystal violet solution. Cells were quantified in five randomly selected fields for each membrane, and the average cell number was used for calculations.

Wound healing

AOX1 KD and vector control cells were plated at 5×10^4 cells/ml in each well of 96-well image lock plate (Essen Bioscience) grown to full confluency and growth-arrested by adding mitomycin 1 ug/mL for 2 h. Following growth-arresting period, the media was replaced and a scratch was made using IncuCyte wound maker. The plates were then incubated in the 37° incubator, 5% CO_2 connected to IncuCyte and images were captured every 2 h using Incu-cyte ZOOM. The images were later analyzed for relative wound density (%) on Integrated cell migration analysis module (Essen Bioscience)

Cell size and morphology analysis

AOX1 KD and vector control cells were fixed, labeled with Alexa 594-conjugated phalloidin for 30 min and imaged with an IC200 (Vala Sciences) high throughput microscope using a Nikon $20 \times /0.75$ Plan Apo VC objective. Image analysis was performed in Matlab (R2016b). In brief, images were binarized using the Otsu's method, and single cells were filtered by size. For each single cell, area, major axis length and minor axis length values were extracted. Cell size and the ratio between the major axis length and the minor axis length were then compared between control ($n = 76$) and knocked down ($n = 159$) cells.

Metabolic flux analysis using U^{13}C-glucose

AOX1 KD (SVH) and Ad-AOX1 (UMCU3) BLCA equal cells (3×10^6) were seeded into 10-cm plates. After 24 h of incubation at 37 °C, the cells were washed twice with glucose-free RPMI containing 10% FBS, 2 mM glutamine, and penicillin-streptomycin. After overnight starvation, 12 mM U^{13}C-glucose (Cambridge isotope laboratories) was added, and cells were incubated for 3 h for glycolysis and 6 h for TCA, PPP metabolites. The plates were then washed with PBS, and snap-frozen in liquid nitrogen. The frozen plates were then used for extraction and LC-MS analysis.

Isotope labeling by targeted MS

Plates were scraped into a 500-μL water:methanol (1:1), sonicated for 1 min (two 30-s pulses) and then mixed with 450 μL ice cold chloroform. The resulting homogenate was then mixed with 150 μL ice cold water and vortex for 2 min. The homogenate was incubated at –20 °C for 30 min and centrifuged at 4 °C for 10 min to partition the aqueous and organic layers. The aqueous and organic layers were combined and dried at 37 °C for 45 min in an automatic environmental speed vac system (GeneVac). The extract was reconstituted in a 500-μL solution of ice cold methanol:

water (1:1) and filtered through a 3-kDa molecular filter (Amicon Ultracel) at 4 °C for 90 min to remove proteins. The filtrate was dried at 37 °C for 45 min in a speed vacuum. For MS analysis, the dried extract was resuspended in a 50-μL solution of methanol:water (1:1) containing 0.1% formic acid and then analyzed using MRM. Solution (10 μL) was injected and analyzed using a 6495 QQQ triple quadrupole mass spectrometer (Agilent Technologies) coupled to a 1290 series HPLC system. Metabolites were targeted in negative ion modes: the electrospray source ionization (ESI) voltage was −3500 V. Approximately 9–12 data points were acquired per detected metabolite. To target the glycolysis, TCA, PPP flux, the samples were delivered to the mass spectrometer via normal phase chromatography using a Luna amino column (3 μm, 100A 2 × 150 mm). The mobile phase containing water (solvent A), with solvent A modified by the addition of 5 mM ammonium acetate (pH 9.9), and 100% acetonitrile (ACN) solvent B). The binary pump flow rate was 0.2 ml/min with a gradient spanning 80% B to 2% A over a 20-min period followed by 2% solvent B to 80% solvent A for a 5-min period and followed by 80% B for 13-min time period. The flow rate was gradually increased during the separation from 0.2 mL/min (0–20 mins), 0.3 mL/min (20.1–25 min), 0.35 mL/min (25–30 min), 0.4 mL/min (30–37.99 min), and finally set at 0.2 mL/min (5 min).

Metabolic flux to measure the nucleosides, nucleotides, and kynurenine

AOX1 KD (SV-HUC-1) and Ad-AOX1 UMCU3 cells were seeded into 10-cm plates. After 24 h at 37 °C, the cells were washed twice with glucose-free RPMI. After overnight starvation, 12 mM U^{13}C-glucose was added and incubated for 72 h. For tryptophan flux 25 μM 15N2 tryptophan was added for 6 h. Cell pellets were stored at −80 °C until the metabolite extraction.

DNA extraction and digestion

Genomic DNA was isolated using Qiagen DNeasy blood and tissue kit, the quantity and quality of the DNA was determined by absorbance using a Biotek microplate reader and digestion procedure was followed from earlier publications [60]. In brief, 1 μg of DNA was denatured by heating at 100 °C for 3 min and subsequently chilled in ice. One-tenth volume of 0.1 M ammonium acetate (pH 5.3) and 2 units of nuclease P1 (Roche Molecular Biochemicals) were added. The mixture was incubated at 45 °C for 2 h. To the solution were subsequently added 1/10 volume of 1 M ammonium bicarbonate and 0.002 units of venom phosphodiesterase I. The incubation was continued for an additional 2 h at 37 °C. Thereafter, the mixture was incubated for 1 h at 37 °C with 0.5 units of alkaline phosphatase. Samples were dried and stored at −80 °C until MS analysis. Prior to MS analysis, the dried extract was resuspended in a 50 μL of methanol:water (1:1) containing 0.1% formic acid and then analyzed using MRM. Targeting the nucleosides and nucleotides, the samples were delivered to the MS via reverse phase chromatography using RRHD SB-CN column (1.8 μm, 3.0 × 100 mm, Agilent Technologies) at 300 μl/min. The initial flow rate was 0.2 ml/min with 2% mobile phase B and 98% mobile phase A. The gradient was set at 2% B at time 0, increased to 5% at 5 min, then increased to 80% at 5.1 min. After that, the gradient was kept at 80% B for 2 min and then decreased to 2% for 3 min. The flow rate was gradually increased during the separation from 0.2 mL/min (0–5 mins), 0.4 mL/min (5.1 to 7 min), 0.2 mL/min (7–10 min), and finally set at 0.2 mL/min (5 min). Buffers A and B were comprised of 0.1% formic acid in water and acetonitrile, respectively.

For ^{13}C labeling experiments, glycolysis, TCA, PPP and nucleosides, and nucleotides expected SRM transitions were calculated for ^{13}C incorporation into various molecules for targeted LC-MS. To assess the validity of our method for calculating isotopomers, we determined the complete isotopomer distribution for each metabolite. Data analysis was performed using Mass Hunter quantitative B.07 software version (Agilent Technologies) and the estimated percent of isotopomer incorporation was calculated using the formula: percent fractional incorporation = ^{13}C/ ^{13}C + ^{12}C × 100 and corrected for isotopomeric distribution and natural abundance.

680C91 Treatment

AOX1 KD and normal bladder epithelium cells were treated with 10 μM TDO2 inhibitor 680C91 (Sigma) for 24 h. After the 24 h, an equal number of cells were collected, processed for the metabolite extraction, and LC-MS analysis.

Kynurenine and NADP measurements

Metabolites extraction procedure adopted from earlier publications [9, 62–65]. The extract was resuspended in an injection solvent, and analyzed by LC-MS. ESI Positive mode was used to separate the metabolites. The LC column was Waters XBridge Amide 3.5 μm, 4.6 × 100 mm. Mobile phase A and B were 0.1% formic acid in water and ACN respectively. Gradient: 0 min-85% B; 0–10 min-85% to 2% B, 10–12 min-2% B, 12–12.1 min-85%-B, followed by re-equilibration end of the gradient–the 4 min to the initial starting condition 85% B. Flow rate: 0.3 ml/min.

Immunofluorescence (IF) microscopy

In all, 2×10^4 AOX1 KD and 1×10^4 Ad-AOX1 UMUC3 cells were seeded in 12-well plates for 48 and 24 h respectively, later cells were fixed in 4% paraformaldehyde for 20 min at room temperature, quenched in 100 mM ammonium chloride and permeabilized with 0.1% TritonX-100 in PBS. After blocking for 1 h in 5% milk/TBST, cells were incubated overnight at 4 °C with rabbit anti-vimentin (1:250, Cell Signaling) or mouse anti-E-cadherin (1:250, Cell Signaling) in TBST/5% milk. After extensive washes, cells were incubated with secondary Alexa647 anti-rabbit (1:1000) or Alexa488 anti-mouse (1:2000) for 1 hour at RT, respectively. Coverslips were mounted with Slow Fade Gold anti-fade reagent (Life Technologies). Images were then acquired on a Biotek Cytation5 image reader using 10X objective, or on a GE Healthcare DeltaVision LIVE high-resolution deconvolution microscope using a 60X plan Apo/1.4 N.A., oil objective.

Western blot

Antibodies to AOX1 (Proteintech, 1:500), EZH2 (BD Biosciences, 1:1000), E-cadherin, vimentin, N-cadherin (Cell Signaling, 1:1,000) and Actin (Sigma, 1:3000), were used. Protein lysates were prepared using RIPA buffer (Sigma) as per the manufacturer's instructions. Secondary anti-rabbit/mouse HRP antibodies (Sigma) were used. Super signal westpico chemiluminescent substrate (Thermo Scientific) used for western blot development.

RNA and qPCR analysis

Standard RNA extraction was carried out by RNeasy Mini Kit (Qiagen), reverse transcription (Quanta Biosciences) and SYBR green (Life Technologies) qPCR were performed. Primers used in this study are listed in Supplementary Table 4.

RNA-seq analysis

Total RNA quality assessment using BioRad Experion Automated Electrophoresis Station and Quantification using Qubit 3.0 fluorometer (Qubit RNA BR Assay Kit). Sample libraries were prepared using the Illumina TruSeq Stranded mRNA Sample Preparation Kit and IDT-TruSeq RNA UD Index, 24 Idx-96 samples. This process purifies the poly A containing mRNA molecules using poly-T oligo attached magnetic beads using two rounds of purification. During the second elution of the poly A RNA, the RNA was also fragmented and primed for cDNA synthesis. DNA was subjected to end repair, A-tailing and adapter ligation. Post ligation cleanup was performed using AMpure XP beads (Agencourt). DNA fragments were amplified using PCR and purified using AMpure XP beads (Agencourt). The quality of the amplified libraries was checked on an Agilent 4200 Tape Station System using the D1000 Screen Tape Assay. The libraries were normalized to 2 nM and pooled (16 samples/flow cell) in equal volumes and sequenced on Illumina NextSeq 550 using Next Seq 500/550 High Output reagent kit V2 (150 cycles). The bcl files were converted to fastq files using Illumina BaseSpace.

In vivo xenograft studies

Animal experiments were performed in accordance with the Baylor College of Medicine (BCM) Institutional Animal Care and Use Committee. Male SCID-Beige fox chase mice (6–8 weeks of age) were obtained from Michael Lewis laboratory at BCM. The mice were used to generate xenografts using SV-HUC-1 cells that were stably transduced with either control shRNA or shRNA targeting AOX1 and Ad-AOX1 UMUC3 and vector control. To generate the xenografts, subcutaneous injection of 100 µL of a mixture containing cells (50 µl of 1×10^6 Ad-AOX1 UMUC3 in 1xDPBS) and 50 µl matrigel (BD Biosciences) was carried out in the hind-flank area of the mice under isoflurane anesthesia. Tumors were measured using calipers thrice per week for a minimum of 4 weeks. Tumor volume was calculated using the formula $TV = (length \times width^2) \times 0.52$ [68]. At the end of the study, the tumors were harvested and flash frozen and later used for metabolomic analysis.

Chorioallantoic membrane assay (CAM)

Fertilized chicken eggs were purchased from Charles River (Norwich, Connecticut, US). The chick chorioallantoic membrane was accessed as previously described [69] on embryonic day 7, and the eggs were inoculated with 5×10^5 UMUC3 control, 100 nM GSK, GSK + Luc and GSK + shAOX1 cells per egg. Photographs of the CAM were taken on 3rd and 5th days of post engraftment. Imaging was conducted on embryonic days 10 and 13, (3 and 5 days after seeding the tumor cells). On the 5th day after inoculation, the eggs were euthanized as per the AVMA guidelines. Tumor size on the CAM was calculated as a percentage of the total area within the inner, 9 mm portion of the silicon ring. In brief, ImageJ was used to manually segment the area occupied by each of the tumors in all groups. The percent tumor area was calculated by dividing the segmented tumor area by the total area within the inner portion of the ring and multiplied by 100. Prism was used to plot the average tumor size per group on a bar graph and to run statistical tests on the data. The CAM tumors were harvested followed by fixed in 10% formalin and embedded in paraffin. To achieve this, the eggshell opening was widened

to allow excision of the CAM and tumor. The paraffin-embedded for used immunohistochemistry (IHC). IHC was performed with AOX1, EZH2, E CAD, N CAD, and Vimentin to check the EMT.

Immuno histochemstry

Tissues were de-paraffinized in xylene and rehydrated in graded alcohols. For antigen retrieval the slide was pressure-cooked for 10 min. Endogenous peroxidase activity was quenched with 3% hydrogen peroxide for 5 min. Slides were blocked by 3% goat serum then incubated with AOX1 antibody (Proteintech, IL), at room temperature for 1 h in humidity chambers. The HRP conjugated goat anti- anti-rabbit secondary antibody (Jackson Immunoresearch Laboratories Inc, West Grove, PA) was applied for 40 min. The antigen–antibody reaction was visualized after diamino-benzidine (Sigma-Aldrich, MO) was applied for 7 min. The slides were counterstained with hematoxylin (Sigma-Aldrich, MO) for 1 min. Positive controls were included in each staining run; negative controls were obtained by omitting the primary antibody. Slides were then dehydrated in alcohols and cleared in three xylene baths before being mounted with Permount (Sigma-Aldrich, MO) media. Stained slides were scanned using Aperio CS2 and analyzed with Aperio positive pixel count algorithm (Leica Biosystems, IL).

Compliance with ethical standards

References

1. Ferlay J, Soerjomataram I, Dikshit R, Eser S, Mathers C, Rebelo M, et al. Cancer incidence and mortality worldwide: sources, methods and major patterns in GLOBOCAN 2012. Int J Cancer. 2015;136:E359–86.
2. Siegel RL, Miller KD, Jemal A. Cancer statistics, 2018. CA Cancer J Clin. 2018;68:7–30.
3. Sievert KD, Amend B, Nagele U, Schilling D, Bedke J, Horstmann M, et al. Economic aspects of bladder cancer: what are the benefits and costs? World J Urol. 2009;27:295–300.
4. Thoma C. Bladder cancer: genomics of noninvasive disease. Nat Rev Urol. 2018;15:1.
5. Hurst CD, Alder O, Platt FM, Droop A, Stead LF, Burns JE, et al. Genomic subtypes of non-invasive bladder cancer with distinct metabolic profile and female gender bias in KDM6A mutation frequency. Cancer Cell. 2017;32:701–15 e7.
6. Garattini E, Fratelli M, Terao M. The mammalian aldehyde oxidase gene family. Hum Genom. 2009;4:119–30.
7. Garattini E, Fratelli M, Terao M. Mammalian aldehyde oxidases: genetics, evolution and biochemistry. Cell Mol Life Sci. 2008;65:1019–48.
8. Kitamura S, Sugihara K, Ohta S. Drug-metabolizing ability of molybdenum hydroxylases. Drug Metab Pharm. 2006;21:83–98.
9. Putluri N, Shojaie A, Vasu VT, Vareed SK, Nalluri S, Putluri V, et al. Metabolomic profiling reveals potential markers and bioprocesses altered in bladder cancer progression. Cancer Res. 2011;71:7376–86.
10. Baylin SB, Herman JG, Graff JR, Vertino PM, Issa JP. Alterations in DNA methylation: a fundamental aspect of neoplasia. Adv Cancer Res. 1998;72:141–96.
11. Merlo A, Herman JG, Mao L, Lee DJ, Gabrielson E, Burger PC, et al. 5' CpG island methylation is associated with transcriptional silencing of the tumour suppressor p16/CDKN2/MTS1 in human cancers. Nat Med. 1995;1:686–92.
12. Esteller M, Tortola S, Toyota M, Capella G, Peinado MA, Baylin SB, et al. Hypermethylation-associated inactivation ofp14(ARF) is independent of p16(INK4a) methylation and p53 mutational status. Cancer Res. 2000;60:129–33.
13. Di Croce L, Helin K. Transcriptional regulation by Polycomb group proteins. Nat Struct Mol Biol. 2013;20:1147–55.
14. Sun S, Yu F, Zhang L, Zhou X. EZH2, an on-off valve in signal network of tumor cells. Cell Signal. 2016;28:481–7.
15. Ma J, Shojaie A, Michailidis G. Network-based pathway enrichment analysis with incomplete network information. Bioinformatics. 2016;32:3165–74.
16. Kim WJ, Kim EJ, Kim SK, Kim YJ, Ha YS, Jeong P, et al. Predictive value of progression-related gene classifier in primary non-muscle invasive bladder cancer. Mol Cancer. 2010;9:3.

17. Cancer Genome Atlas Research Network Comprehensive molecular characterization of urothelial bladder carcinoma. Nature. 2014;507:315–22.
18. Sanchez-Carbayo M, Socci ND, Lozano J, Saint F, Cordon-Cardo C. Defining molecular profiles of poor outcome in patients with invasive bladder cancer using oligonucleotide microarrays. J Clin Oncol. 2006;24:778–89.
19. Choi W, Porten S, Kim S, Willis D, Plimack ER, Hoffman-Censits J, et al. Identification of distinct basal and luminal subtypes of muscle-invasive bladder cancer with different sensitivities to frontline chemotherapy. Cancer Cell. 2014;25:152–65.
20. McCabe MT, Ott HM, Ganji G, Korenchuk S, Thompson C, Van Aller GS, et al. EZH2 inhibition as a therapeutic strategy for lymphoma with EZH2-activating mutations. Nature. 2012;492:108–12.
21. Vire E, Brenner C, Deplus R, Blanchon L, Fraga M, Didelot C, et al. The Polycomb group protein EZH2 directly controls DNA methylation. Nature. 2006;439:871–4.
22. Kleer CG, Cao Q, Varambally S, Shen R, Ota I, Tomlins SA, et al. EZH2 is a marker of aggressive breast cancer and promotes neoplastic transformation of breast epithelial cells. Proc Natl Acad Sci USA. 2003;100:11606–11.
23. Oster B, Thorsen K, Lamy P, Wojdacz TK, Hansen LL, Birkenkamp-Demtroder K, et al. Identification and validation of highly frequent CpG island hypermethylation in colorectal adenomas and carcinomas. Int J Cancer. 2011;129:2855–66.
24. Salter M, Pogson CI. The role of tryptophan 2,3-dioxygenase in the hormonal control of tryptophan metabolism in isolated rat liver cells. Effects of glucocorticoids and experimental diabetes. Biochem J. 1985;229:499–504.
25. D'Amato NC, Rogers TJ, Gordon MA, Greene LI, Cochrane DR, Spoelstra NS, et al. A TDO2-AhR signaling axis facilitates anoikis resistance and metastasis in triple-negative breast cancer. Cancer Res. 2015;75:4651–64.
26. Yang J, Weinberg RA. Epithelial-mesenchymal transition: at the crossroads of development and tumor metastasis. Dev Cell. 2008;14:818–29.
27. De Craene B, Berx G. Regulatory networks defining EMT during cancer initiation and progression. Nat Rev Cancer. 2013;13:97–110.
28. Deryugina EI, Quigley JP. Chick embryo chorioallantoic membrane model systems to study and visualize human tumor cell metastasis. Histochem Cell Biol. 2008;130:1119–30.
29. Kompier LC, Lurkin I, van der Aa MN, van Rhijn BW, van der Kwast TH, Zwarthoff EC. FGFR3, HRAS, KRAS, NRAS and PIK3CA mutations in bladder cancer and their potential as biomarkers for surveillance and therapy. PLoS ONE. 2010;5:e13821.
30. Vantaku V, Dong J, Ambati CR, Perera D, Donepudi SR, Amara CS, et al. Multi-omics integration analysis robustly predicts high-grade patient survival and identifies CPT1B effect on fatty acid metabolism in Bladder Cancer. Clin Cancer Res. 2019;15:3689–701.
31. Platten M, Wick W, Van den Eynde BJ. Tryptophan catabolism in cancer: beyond IDO and tryptophan depletion. Cancer Res. 2012;72:5435–40.
32. Ablain J, de The H. Retinoic acid signaling in cancer: the parable of acute promyelocytic leukemia. Int J Cancer. 2014;135:2262–72.
33. Yang M, Pollard PJ. Succinate: a new epigenetic hacker. Cancer Cell. 2013;23:709–11.
34. Zhai L, Spranger S, Binder DC, Gritsina G, Lauing KL, Giles FJ, et al. Molecular pathways: targeting IDO1 and other tryptophan dioxygenases for cancer immunotherapy. Clin Cancer Res. 2015;21:5427–33.
35. Icard P, Poulain L, Lincet H. Understanding the central role of citrate in the metabolism of cancer cells. Biochim Biophys Acta. 2012;1825:111–6.
36. Ozturk S, Papageorgis P, Wong CK, Lambert AW, Abdolmaleky HM, Thiagalingam A, et al. SDPR functions as a metastasis suppressor in breast cancer by promoting apoptosis. Proc Natl Acad Sci USA. 2016;113:638–43.
37. Haldrup C, Mundbjerg K, Vestergaard EM, Lamy P, Wild P, Schulz WA, et al. DNA methylation signatures for prediction of biochemical recurrence after radical prostatectomy of clinically localized prostate cancer. J Clin Oncol. 2013;31:3250–8.
38. Park JS, Choi SB, Chung JW, Kim SW, Kim DW. Classification of serous ovarian tumors based on microarray data using multicategory support vector machines. Conf Proc IEEE Eng Med Biol Soc. 2014;2014:3430–3.
39. Varambally S, Dhanasekaran SM, Zhou M, Barrette TR, Kumar-Sinha C, Sanda MG, et al. The polycomb group protein EZH2 is involved in progression of prostate cancer. Nature. 2002;419:624–9.
40. Bachmann IM, Halvorsen OJ, Collett K, Stefansson IM, Straume O, Haukaas SA, et al. EZH2 expression is associated with high proliferation rate and aggressive tumor subgroups in cutaneous melanoma and cancers of the endometrium, prostate, and breast. J Clin Oncol. 2006;24:268–73.
41. Sudo T, Utsunomiya T, Mimori K, Nagahara H, Ogawa K, Inoue H, et al. Clinicopathological significance of EZH2 mRNA expression in patients with hepatocellular carcinoma. Br J Cancer. 2005;92:1754–8.
42. Hussain M, Rao M, Humphries AE, Hong JA, Liu F, Yang M, et al. Tobacco smoke induces polycomb-mediated repression of Dickkopf-1 in lung cancer cells. Cancer Res. 2009;69:3570–8.
43. Yan J, Ng SB, Tay JL, Lin B, Koh TL, Tan J, et al. EZH2 overexpression in natural killer/T-cell lymphoma confers growth advantage independently of histone methyltransferase activity. Blood. 2013;121:4512–20.
44. Tan JZ, Yan Y, Wang XX, Jiang Y, Xu HE. EZH2: biology, disease, and structure-based drug discovery. Acta Pharmacol Sin. 2014;35:161–74.
45. The EZH2 Inhibitor Tazemetostat Is Well Tolerated in a Phase I Trial. Cancer Discov. 2018;8:OF15. http://cancerdiscovery.aacrjournals.org/content/early/2018/04/20/2159-8290.CD-RW2018-067, https://doi.org/10.1158/2159-8290.CD-RW2018-067. Accessed 9 Apr 2018.
46. Kim KH, Roberts CW. Targeting EZH2 in cancer. Nat Med. 2016;22:128–34.
47. Dudziec E, Goepel JR, Catto JW. Global epigenetic profiling in bladder cancer. Epigenomics. 2011;3:35–45.
48. Reinert T, Modin C, Castano FM, Lamy P, Wojdacz TK, Hansen LL, et al. Comprehensive genome methylation analysis in bladder cancer: identification and validation of novel methylated genes and application of these as urinary tumor markers. Clin Cancer Res. 2011;17:5582–92.
49. Wolff EM, Chihara Y, Pan F, Weisenberger DJ, Siegmund KD, Sugano K, et al. Unique DNA methylation patterns distinguish noninvasive and invasive urothelial cancers and establish an epigenetic field defect in premalignant tissue. Cancer Res. 2010;70:8169–78.
50. Agledal L, Niere M, Ziegler M. The phosphate makes a difference: cellular functions of NADP. Redox Rep. 2010;15:2–10.
51. Ying W. NAD+/NADH and NADP+/NADPH in cellular functions and cell death: regulation and biological consequences. Antioxid Redox Signal. 2008;10:179–206.
52. Prendergast GC. Cancer: why tumours eat tryptophan. Nature. 2011;478:192–4.
53. Chen Y, Guillemin GJ. Kynurenine pathway metabolites in humans: disease and healthy States. Int J Tryptophan Res. 2009;2:1–19.
54. Chalkiadaki A, Guarente L. The multifaceted functions of sirtuins in cancer. Nat Rev Cancer. 2015;15:608–24.
55. Beaconsfield P, Ginsburg J, Jeacock MK. Glucose metabolism via the pentose phosphate pathway relative to nucleic acid and protein synthesis in the human placenta. Dev Med Child Neurol. 1964;6:469–74.
56. Davidson B, Abeler VM, Forsund M, Holth A, Yang Y, Kobayashi Y, et al. Gene expression signatures of primary and metastatic uterine leiomyosarcoma. Hum Pathol. 2014;45:691–700.

57. Opitz CA, Litzenburger UM, Sahm F, Ott M, Tritschler I, Trump S, et al. An endogenous tumour-promoting ligand of the human aryl hydrocarbon receptor. Nature. 2011;478:197–203.

58. Minn AJ, Gupta GP, Siegel PM, Bos PD, Shu W, Giri DD, et al. Genes that mediate breast cancer metastasis to lung. Nature. 2005;436:518–24.

59. Bos PD, Zhang XH, Nadal C, Shu W, Gomis RR, Nguyen DX, et al. Genes that mediate breast cancer metastasis to the brain. Nature. 2009;459:1005–9.

60. Jin F, Thaiparambil J, Donepudi SR, Vantaku V, Piyarathna DWB, Maity S, et al. Tobacco-specific carcinogens induce hypermethylation, DNA adducts, and DNA damage in bladder cancer. Cancer Prev Res. 2017;10:588–97.

61. Piyarathna DWB, Rajendiran TM, Putluri V, Vantaku V, Soni T, von Rundstedt FC, et al. Distinct lipidomic landscapes associated with clinical stages of urothelial cancer of the bladder. Eur Urol Focus. 2018;4:907–915.

62. Terunuma A, Putluri N, Mishra P, Mathe EA, Dorsey TH, Yi M, et al. MYC-driven accumulation of 2-hydroxyglutarate is associated with breast cancer prognosis. J Clin Invest. 2014;124:398–412.

63. Putluri N, Maity S, Kommagani R, Creighton CJ, Putluri V, Chen F, et al. Pathway-centric integrative analysis identifies RRM2 as a prognostic marker in breast cancer associated with poor survival and tamoxifen resistance. Neoplasia. 2014;16:390–402.

64. Putluri N, Shojaie A, Vasu VT, Nalluri S, Vareed SK, Putluri V, et al. Metabolomic profiling reveals a role for androgen in activating amino acid metabolism and methylation in prostate cancer cells. PLoS ONE. 2011;6:e21417.

65. Bhowmik SK, Ramirez-Pena E, Arnold JM, Putluri V, Sphyris N, Michailidis G, et al. EMT-induced metabolite signature identifies poor clinical outcome. Oncotarget. 2015;6:42651–60.

66. Estecio MR, Yan PS, Ibrahim AE, Tellez CS, Shen L, Huang TH, et al. High-throughput methylation profiling by MCA coupled to CpG island microarray. Genome Res. 2007;17:1529–36.

67. Blecher-Gonen R, Barnett-Itzhaki Z, Jaitin D, Amann-Zalcenstein D, Lara-Astiaso D, Amit I. High-throughput chromatin immuno-precipitation for genome-wide mapping of in vivo protein-DNA interactions and epigenomic states. Nat Protoc. 2013;8:539–54.

68. O'Reilly MS, Boehm T, Shing Y, Fukai N, Vasios G, Lane WS, et al. Endostatin: an endogenous inhibitor of angiogenesis and tumor growth. Cell. 1997;88:277–85.

69. Li M, Pathak RR, Lopez-Rivera E, Friedman SL, Aguirre-Ghiso JA, Sikora AG. The in ovo chick chorioallantoic membrane (CAM) assay as an efficient xenograft model of hepatocellular carcinoma. J Vis Exp. 2015.